

KUNS-1533, OU-TAP 84, YITP-98-65

Low frequency gravitational waves from black hole MACHO binaries

Kunihiro Ioka,¹ Takahiro Tanaka,² and Takashi Nakamura³¹ *Department of Physics, Kyoto University, Kyoto 606-8502, Japan*² *Department of Earth and Space Science, Osaka University, Toyonaka 560, Japan*³ *Yukawa Institute for Theoretical Physics, Kyoto University, Kyoto 606-8502, Japan*

(January 8, 2019)

Abstract

The intensity of low frequency gravitational waves from black hole MACHO binaries is studied. First we estimate the gravitational wave background produced by black hole MACHO binaries in the Milky Way halo as well as the cosmological gravitational wave background produced by the extragalactic black hole MACHO binaries. It is found that the cosmological gravitational wave background due to black hole MACHO binaries is larger than the halo background unless an extreme model of the halo is assumed, while it is smaller than the background due to close white dwarf binaries at $\nu_{gw} \lesssim 10^{-2.5}$ Hz if the actual space density of white dwarfs is maximal. This cosmological background due to black hole MACHO binaries is well below the observational constraints from the pulsar timing, quasar proper motions and so on. We find that one year observation by LISA will be able to detect gravitational waves from at least several hundreds of nearby independent black hole MACHO binaries whose amplitudes exceed these backgrounds. This suggests that LISA will be able to pin down various properties of primordial black hole MACHOs

together with the results of LIGO-VIRGO-TAMA-GEO network. Furthermore, it may be possible to draw a map of the mass distribution of our halo, since LISA can determine the position and the distance to individual sources consisted of black hole MACHO binaries. Therefore, LISA may open a new field of the gravitational wave astronomy.

PACS numbers: 98.80.-k, 04.30.-w, 97.60.Lf, 95.35.+d

I. INTRODUCTION

The observations of gravitational microlensing toward the Large Magellanic Cloud (LMC) have revealed that a significant fraction of the Milky Way halo consists of solar or sub-solar-mass compact objects, which are called massive compact halo objects (MACHOs). The analysis of the first 2.1 years of photometry of 8.5×10^6 stars in the LMC by the MACHO Collaboration [1] suggests that the fraction $0.62^{+0.3}_{-0.2}$ of the halo consists of MACHOs of mass $0.5^{+0.3}_{-0.2} M_\odot$ assuming the standard spherical flat rotation halo model. The preliminary analysis of four years of data suggests the existence of eight additional microlensing events with $t_{dur} \sim 90$ days in the direction of the LMC [2].

At present, we do not know what MACHOs are. This is especially because there are strong degeneracies in any microlensing measurements among the mass, the velocity and the distance to a lens object. There are several candidates proposed to explain MACHOs. However, all of them have some theoretical or observational difficulties. The inferred mass is just the mass of red dwarfs. However, observationally there is a tight constraint on the mass fraction of red dwarfs to the total mass of the halo [3–5]. Red dwarfs can contribute to, at most, a few percent of the total mass of the halo. The possibility that the MACHOs are neutron stars is ruled out by the observational constraints on the metal and helium abundance [6]. If MACHOs are white dwarfs, the initial mass function (IMF) must have been peaked around $\sim 2M_\odot$ when they formed [7–9], which IMF is completely different from the present day IMF. Furthermore, assuming the Salpeter IMF with an upper and a lower mass cutoff, the mass fraction of the white dwarfs in the halo should be less than 10 % from the number count of high z galaxies [10]. The observation of the chemical yield also disfavors MACHOs being white dwarfs [11,12]. Brown dwarfs are possible candidates for MACHOs [13], since they are free from problems concerning metals and star counts. However, they require both a non-standard halo model and a mass function concentrated close to the hydrogen burning limit. Extrapolating the mass function of red dwarfs, we find that the contribution of brown dwarfs to the mass of the halo is less than a few percent [5,14]. In any case, extreme param-

eters or models are needed as long as white dwarf/brown dwarf MACHOs are concerned, although future observations of the high velocity white dwarfs/brown dwarfs in our solar neighborhood might prove the existence of white dwarf/brown dwarf MACHOs (see also [15]).

Measurements of the optical depth in other lines of sight, including SMC and M31, are needed to confirm that MACHOs exist everywhere in the halo. One microlensing event toward SMC [16,17] is not sufficient to determine the optical depth toward SMC reliably. Since only the optical depth toward the LMC is available at present, in principle there is the possibility that MACHOs do not exist in other lines of sight. Any objects clustered somewhere between the LMC and the sun with the column density larger than $25M_{\odot}\text{pc}^{-2}$ [18] can explain the data. They include the possibilities; LMC-LMC self-lensing, the spheroid component, the thick disk, a dwarf galaxy, the tidal debris, warping and flaring of the Galactic disk [19–22]. However, none of them do not convincingly explain the microlensing events toward the LMC. This means that it is worth considering alternative possibilities that MACHOs are not stellar objects but absolutely new objects such as black holes of mass $\sim 0.5M_{\odot}$ or boson stars with the boson mass of $\sim 10^{-10}\text{eV}$.

In this paper, we consider primordial black holes to explain MACHOs. This possibility is free from observational constraints at present. Theoretically it is still uncertain if black holes are formed in the early universe in spite of several arguments on the formation mechanisms of primordial black holes [23–25]. Our standpoint here is not to discuss the details of the formation mechanism but to establish the observational signatures of primordial black holes if they exist. Firstly, electromagnetic radiation from gas accreting to a black hole MACHO (BHMACHO) is too dim to be observed unless the velocity of BHMACHOs is exceptionally small [26]. If primordial black holes are formed, most of them evolve into binaries through the three body interaction in the early universe at $t \sim 10^{-5}\text{s}$ [27,28]. Some of these BHMACHO binaries coalesce at or before present epoch and it may be possible to detect the gravitational waves from such coalescing BHMACHO binaries. The event rate of coalescing BHMACHO binaries is estimated as $5 \times 10^{-2} \times 2^{\pm 1}$ events/yr/galaxy, which suggests that we can detect

several events per year within 15 Mpc by LIGO-VIRGO-TAMA-GEO network [27,28].

On the other hand, the other part of BHMACHO binaries still have large separations, and they emit gravitational waves at lower frequencies. These low frequency gravitational waves may be detected by the planned Laser Interferometer Space Antenna (LISA), which will be sensitive to gravitational waves in the frequency band of $10^{-4} - 10^{-1}$ Hz. In this paper, we investigate low frequency gravitational waves emitted by BHMACHO binaries, and we argue that LISA will be able to detect gravitational waves from BHMACHO binaries.

In Sec. II we review the formation scenario of BHMACHO binaries proposed in Ref. [27,28]. In Sec. III we establish a method to estimate the probability distribution function of the binary parameters as a function of the age after the binary formation, t . In Sec. IV we calculate the gravitational wave background produced by BHMACHO binaries in the Milky Way halo. In Sec. V we obtain the cosmological gravitational wave background produced by extragalactic BHMACHO binaries. We also compare the amplitude of the cosmological gravitational wave background produced by BHMACHO binaries with the observational constraints such as the pulsar timing and quasar proper motions. In Sec. VI, taking into account other noise sources in the LISA detection band, such as instrumental noises and the background produced by close white dwarf binaries (CWDBs), we summarize the spectral density of all noises in terms of the gravitational wave amplitude. In Sec. VII we estimate how many nearby BHMACHO binaries are expected to be observed by LISA. Section VIII is devoted to summary and discussion.

II. FORMATION SCENARIO OF BHMACHO BINARIES

We briefly review the formation scenario of BHMACHO binaries given in Ref. [27,28] to introduce our notations. For simplicity, we assume that black holes dominate the dark matter, i.e., $\Omega = \Omega_{BH}$, where Ω_{BH} is the density parameter of BHMACHOs at present. Furthermore, we assume that all black holes have the same mass M_{BH} . We normalize the scale factor such that $R = 1$ at the time of matter-radiation equality.

Primordial black holes are formed when the horizon scale is comparable to the Schwarzschild radius of the black holes [29]. The scale factor at the time of the black hole formation is given by

$$R_f = \sqrt{\frac{GM_{BH}}{c^3 H_{eq}^{-1}}} = 1.1 \times 10^{-8} \left(\frac{M_{BH}}{M_\odot} \right)^{1/2} (\Omega h^2), \quad (2.1)$$

where H_{eq} is the Hubble parameter at the time of matter-radiation equality, i.e., $cH_{eq}^{-1} = \sqrt{3c^2/8\pi G\rho_{eq}} = 1.2 \times 10^{21}(\Omega h^2)^{-2}$ cm. The mean separation of black holes at the time of matter-radiation equality is given by

$$\bar{x} = (M_{BH}/\rho_{eq})^{1/3} = 1.2 \times 10^{16} (M_{BH}/M_\odot)^{1/3} (\Omega h^2)^{-4/3} \text{ [cm]}. \quad (2.2)$$

Consider a pair of black holes with the same mass M_{BH} and a comoving separation $x < \bar{x}$. We define an averaged energy density of this pair of black holes by dividing their masses by the volume of a sphere whose comoving radius equals to x as $\bar{\rho}_{BH} \equiv \rho_{eq}\bar{x}^3/(x^3 R^3)$. Then, $\bar{\rho}_{BH}$ becomes larger than the mean radiation energy density, $\rho_R = \rho_{eq}/R^4$, when

$$R > R_m \equiv \left(\frac{x}{\bar{x}} \right)^3. \quad (2.3)$$

After $R = R_m$, the motion of the pair is decoupled from the cosmic expansion, and the pair forms a binary. Unless x is exceptionally small, this newly formed binary is kept from colliding with each other by the effect of tidal force from neighboring black holes, which gives the binary sufficiently large angular momentum.

The initial value of the semimajor axis a will be proportional to xR_m , and hence

$$a = \alpha x R_m = \alpha \frac{x^4}{\bar{x}^3}, \quad (2.4)$$

where α is a constant of order unity. To estimate the tidal torque, we assume that the tidal force is dominated by the black hole that is nearest to the binary. We use y to represent the comoving separation of the nearest neighboring black hole from the center of mass of the binary. Then, the semiminor axis, b , will be proportional to (tidal force) \times (free fall time) 2 , and hence it is given by

$$b = \alpha \beta \frac{M_{BH} x R_m}{(y R_m)^3} \frac{(x R_m)^3}{M_{BH}} = \beta \left(\frac{x}{y} \right)^3 a, \quad (2.5)$$

where β is a constant of order unity. Then, the binary's eccentricity, e , is evaluated by

$$e = \sqrt{1 - \beta^2 \left(\frac{x}{y} \right)^6}. \quad (2.6)$$

In Ref. [28], it is verified that the analytic estimates given in Eqs. (2.4) and (2.5) are good approximations and the numerical coefficients, α and β , are actually of order unity. In this paper, we adopt $\alpha = 0.5$ and $\beta = 0.7$. ¹

If we assume that black holes are distributed randomly, the probability distribution function, $P(x, y)$, for the initial comoving separation of the binary, x , and the initial comoving separation of the nearest neighboring black hole from the center of mass of the binary, y , is given by

$$P(x, y) dx dy = \frac{9x^2 y^2}{\bar{x}^6} e^{-y^3/\bar{x}^3} dx dy, \quad (2.7)$$

where $0 < x < y < \infty$. This probability distribution function is normalized to satisfy $\int_0^\infty dx \int_x^\infty dy P(x, y) = 1$. Changing the variables x and y in Eq. (2.7) to a and e with Eqs. (2.4) and (2.6), we obtain the probability distribution function for the eccentricity and the semimajor axis of binaries as

$$f(a, e) da de = \frac{3}{4} \frac{\beta}{(\alpha \bar{x})^{3/2}} \frac{a^{1/2} e}{(1 - e^2)^{3/2}} \exp \left[-\frac{\beta}{(1 - e^2)^{1/2}} \left(\frac{a}{\alpha \bar{x}} \right)^{3/4} \right] da de, \quad (2.8)$$

where $\sqrt{1 - \beta^2} < e < 1$ and $0 < a < \infty$. Note that $f(a, e) = 0$ for $0 < e < \sqrt{1 - \beta^2}$.

We consider here BHMACHO binaries whose period of orbital motion is short. Their coalescence time due to the emission of gravitational waves is approximately given by [30]

¹ In Ref. [28], $\alpha = 0.4$ and $\beta = 0.8$ are adopted. However, these values are obtained by a least squares fitting without fixing the power indices of a and b . When we use the power indices of the analytical estimates, i.e., 3 for a and 4 for b , it is better to adopt $\alpha = 0.5$ and $\beta = 0.7$. Note that the results of this paper are not affected so much by the detailed choice of these constants.

$$t = t_0 \left(\frac{a}{a_0} \right)^4 (1 - e^2)^{\frac{7}{2}}, \quad a_0 = 2.0 \times 10^{11} \left(\frac{M_{BH}}{M_\odot} \right)^{\frac{3}{4}} [\text{cm}] \quad (2.9)$$

where $t_0 = 10^{10} \text{yr}$ and a_0 is the semimajor axis of a binary in a circular orbit which coalesces in t_0 . Using Eqs. (2.4) and (2.6), Eq. (2.9) can be written in terms of x and y as

$$t = \bar{t} \left(\frac{x}{\bar{x}} \right)^{37} \left(\frac{y}{\bar{x}} \right)^{-21}, \quad \bar{t} = \beta^7 \left(\frac{\alpha \bar{x}}{a_0} \right)^4 t_0. \quad (2.10)$$

Integrating Eq. (2.7) for a given t with the aid of Eq. (2.10), we obtain the probability distribution function for the coalescence time $f_t(t)$. We should take the range of the integration to satisfy $0 < x < \bar{x}$ and $x < y < \infty$. The first condition ($x < \bar{x}$) is necessary for the pair to be a binary. The second condition turns out to be $(t/\bar{t})^{1/16} \bar{x} < y < (t/\bar{t})^{-1/21} \bar{x}$ for a fixed t . Performing the integration, we obtain

$$\begin{aligned} f_t(t) dt &= \frac{3}{37} \left(\frac{t}{\bar{t}} \right)^{3/37} \left[\Gamma \left(\frac{58}{37}, \left(\frac{t}{\bar{t}} \right)^{3/16} \right) - \Gamma \left(\frac{58}{37}, \left(\frac{t}{\bar{t}} \right)^{-1/7} \right) \right] \frac{dt}{t} \\ &\cong \frac{3}{37} \left(\frac{t}{\bar{t}} \right)^{3/37} \Gamma \left(\frac{58}{37} \right) \frac{dt}{t}, \end{aligned} \quad (2.11)$$

where $\Gamma(x, a)$ is the incomplete gamma function defined by

$$\Gamma(x, a) = \int_a^\infty s^{x-1} e^{-s} ds, \quad (2.12)$$

and $\Gamma(58/37) = 0.890 \dots$. The second equality in Eq. (2.11) is valid when $t/\bar{t} \ll 1$. This is automatically satisfied as long as we consider the case $t \sim t_0$ with typical values of parameters, for which $t_0/\bar{t} \ll 1$ is satisfied.

III. LATE TIME DISTRIBUTION OF THE BINARY PARAMETERS

A. numerical approach

Since a BHMACHO binary radiates gravitational waves, the binary parameters change as a function of time due to radiation reaction. The probability distribution function, $f(a, e)$, in Eq. (2.8) is also a function of time. In this section, we develop a method to compute this

time dependent distribution function, $f(a, e; t_1)$, where t_1 is the time after the formation of binaries. We refer to the initial values of a and e as a_i and e_i , respectively.

Firstly, we represent a_i and e_i as a function of the present values of binary orbital parameters, a and e , and the component masses of the binary, M_{BH1} and M_{BH2} . The formula that relates e_i to e is given in Ref. [30] by

$$\frac{19\mathcal{B}t_1}{12c_0^4} = \int_e^{e_i} \frac{de}{(1-e^2)^{3/2}} \frac{e^{29/19} [1 + (121/304)e^2]^{1181/2299}}{[1 + (121/304)e^2]^{1181/2299}} =: \mathcal{I}, \quad (3.1)$$

where

$$\mathcal{B} = \frac{64}{5} \frac{G^3 M_{BH1} M_{BH2} (M_{BH1} + M_{BH2})}{c^5}, \quad (3.2)$$

and

$$c_0 = a_i e_i^{-12/19} (1 - e_i^2) \left[1 + \frac{121}{304} e_i^2 \right]^{-870/2299} = a e^{-12/19} (1 - e^2) \left[1 + \frac{121}{304} e^2 \right]^{-870/2299}. \quad (3.3)$$

Using the above relations, we can determine a_i and e_i as a function of a, e and t_1 numerically. We can also obtain a_i and e_i , by numerically integrating the evolution equations [30],

$$\frac{da}{dt} = -\frac{\mathcal{B}}{a^3 (1 - e^2)^{7/2}} \left(1 + \frac{73}{24} e^2 + \frac{37}{96} e^4 \right), \quad \frac{de}{dt} = -\frac{19}{12} \frac{\mathcal{B} e}{a^4 (1 - e^2)^{5/2}} \left(1 + \frac{121}{304} e^2 \right), \quad (3.4)$$

from the present time backward to the initial time.

Secondly, we need to calculate the Jacobian to relate the distribution of a and e with that of a_i and e_i . For this purpose, we take the total differentiation of Eqs. (3.1) and (3.3) to obtain

$$\begin{aligned} \frac{da}{a} - \frac{12}{19} \frac{1 + (73/24)e^2 + (37/96)e^4}{(1 - e^2)[1 + (121/304)e^2]} \frac{de}{e} &= \frac{da_i}{a_i} - \frac{12}{19} \frac{1 + (73/24)e_i^2 + (37/96)e_i^4}{(1 - e_i^2)[1 + (121/304)e_i^2]} \frac{de_i}{e_i}, \\ -4 \left[\frac{da}{a} - \frac{12}{19} \frac{1 + (73/24)e^2 + (37/96)e^4}{(1 - e^2)[1 + (121/304)e^2]} \frac{de}{e} \right] + \frac{e^{29/19} [1 + (121/304)e^2]^{1181/2299}}{(1 - e^2)^{3/2}} \frac{de}{\mathcal{I}} &= \frac{e_i^{29/19} [1 + (121/304)e_i^2]^{1181/2299}}{(1 - e_i^2)^{3/2}} \frac{de_i}{\mathcal{I}}. \end{aligned} \quad (3.5)$$

Then, by taking the wedge product of the above two equations, we easily find the Jacobian relation,

$$\frac{da}{a} \frac{e^{29/19} [1 + (121/304)e^2]^{1181/2299}}{(1 - e^2)^{3/2}} de = \frac{da_i}{a_i} \frac{e_i^{29/19} [1 + (121/304)e_i^2]^{1181/2299}}{(1 - e_i^2)^{3/2}} de_i. \quad (3.6)$$

Since the distribution function $f(a, e; t_1)$ at a time t_1 is related to the initial distribution function $f_i(a_i, e_i)$ by

$$f(a, e; t_1) da de = f_i(a_i, e_i) da_i de_i, \quad (3.7)$$

we find

$$f(a, e; t_1) = \frac{a_i}{a} \left(\frac{e}{e_i} \right)^{29/19} \left(\frac{1 - e_i^2}{1 - e^2} \right)^{3/2} \left[\frac{1 + (121/304)e^2}{1 + (121/304)e_i^2} \right]^{1181/2299} f_i(a_i, e_i), \quad (3.8)$$

where $f_i(a_i, e_i)$ is given by Eq. (2.8).

The Keplerian orbital frequency of a binary, ν_p , is related to the length of the semimajor axis, a , by

$$2\pi\nu_p = \sqrt{\frac{G(M_{BH1} + M_{BH2})}{a^3}}, \quad (3.9)$$

where we add the subscript, p , to the orbital frequency, ν , for later convenience. Hence, the distribution function for a and e is transformed into that for ν_p and e by

$$f_{\nu, e, t}(\nu_p, e; t_1) = f(a, e; t_1) \left| \frac{da}{d\nu_p} \right| = \frac{2a}{3\nu_p} f(a, e; t_1). \quad (3.10)$$

In Fig. 1, we plot $f_{\nu, e, t}(\nu_p, e; t_1)$ for $t_1 = t_0 = 10^{10}$ yr as a function of e for several orbital frequencies. Here we adopt $M_{BH} = 0.5M_\odot$ and $\Omega h^2 = 0.1$. As we can see in Fig. 1, binaries with a high orbital frequency ($\nu_p \gtrsim 10^{-3}$ Hz) are almost in circular orbits at present, while binaries with a low orbital frequency ($\nu_p \lesssim 10^{-3}$ Hz) keep their eccentricity large even now. The transition frequency from an eccentric orbit to a circular one depends on M_{BH} , Ωh^2 and t_1 . Note that almost all binaries formed through the mechanism presented in Section. II are eccentric when they are formed, as we can see from Eq. (2.6).

B. approximate formula

An approximate formula for the distribution function of ν_p can be obtained in the case that the eccentricity has already decayed at a time t_1 . Under the assumption $e \ll 1$, the remaining time before a binary with the semimajor axis, a , coalesces is given by [30]

$$\Delta t = \frac{425}{768} t_0 \frac{a^4}{a_0^4}, \quad (3.11)$$

where a_0 is given in Eq. (2.9) and $t_0 = 10^{10}$ yr. On the other hand, the distribution function of coalescence time is given by Eq. (2.11), which can be interpreted as the distribution function of Δt by replacing t with $t_1 + \Delta t$. Then, by using Eqs. (3.9) and (3.11), we obtain an approximate formula for the distribution function of the orbital frequency as

$$f_{\nu,t}(\nu_p; t_1) d\nu_p \sim \frac{425}{3552} \left(\frac{t_1}{\bar{t}}\right)^{3/37} \frac{t_0}{t_1} \left(\frac{a}{a_0}\right)^4 \Gamma\left(\frac{58}{37}\right) \frac{d\nu_p}{\nu_p}, \quad (3.12)$$

where we assume $t_1 \gg \Delta t$. This expression corresponds to the quantity that is obtained by integrating the distribution function $f_{\nu,e,t}(\nu_p, e; t_1)$ in Eq. (3.10) over e . Since the semimajor axis, a , is proportional to $\nu_p^{-2/3}$ in Eq. (3.9), we find

$$f_{\nu,t}(\nu_p; t_1) \propto \nu_p^{-11/3}. \quad (3.13)$$

On the other hand, we have $a_0 \propto M_{BH}^{3/4}$ from Eq. (2.9), $a \propto M_{BH}^{1/3}$ from Eq. (3.9), and $\bar{t} \propto M_{BH}^{-5/3}(\Omega h^2)^{16/3}$ from Eqs. (2.2), (2.9) and (2.10). Then, for a fixed orbital frequency, we find there is a relation

$$f_{\nu,t}(\nu_p; t_1) \propto M_{BH}^{-170/111}(\Omega h^2)^{16/37}. \quad (3.14)$$

IV. GRAVITATIONAL WAVE BACKGROUND PRODUCED BY BHMACHO BINARIES IN THE MILKY WAY HALO

In this section, we investigate gravitational wave background produced by BHMACHO binaries in the Milky Way halo. In our model, there are so many BHMACHO binaries in our galaxy that they themselves become stochastic background sources, and may limit the confusion noise level for individual sources.

A. gravitational waves from two point masses in a Keplerian orbit

A circular orbit binary emits gravitational waves only at a frequency $\nu_{gw} = 2\nu_p$. However, a binary with eccentricity $e \neq 0$ emits gravitational waves at frequencies $\nu_{gw} = p\nu_p$ ($p =$

$1, 2, \dots$) [31,32]. As we have seen at the end of Section III A, almost all binaries formed through the mechanism explained in Section II are highly eccentric when they are formed, and orbits of binaries with a low orbital frequency still remain eccentric even at present. Therefore, the contribution from high harmonics may be important.

Gravitational waves at frequency ν_{gw} are emitted by binaries whose present Keplerian frequency is

$$\nu_p = \nu_{gw}/p, \quad (p = 1, 2, \dots). \quad (4.1)$$

The gravitational wave luminosity from a binary which emits gravitational waves at frequency ν_{gw} as the p -th harmonic is given by [31]

$$L^{(p)}(\nu_{gw}, e) = L_0 \nu_{gw}^{10/3} p^{-10/3} g(p, e), \quad (4.2)$$

where

$$L_0 = 1.351 \times 10^{44} \left(\frac{M_{BH1} M_{BH2} / (M_{BH1} + M_{BH2})}{M_\odot / 4} \right)^2 \left(\frac{M_{BH1} + M_{BH2}}{M_\odot} \right)^{4/3} \quad [\text{erg s}^{-1} \text{ Hz}^{-10/3}], \quad (4.3)$$

and M_{BH1} and M_{BH2} are component masses of the binary. The function $g(p, e)$ is given by [31]

$$g(p, e) = \frac{p^4}{32} \left\{ \left[J_{p-2}(pe) - 2eJ_{p-1}(pe) + \frac{2}{p} J_p(pe) + 2eJ_{p+1}(pe) - J_{p+2}(pe) \right]^2 + (1 - e^2) [J_{p-2}(pe) - 2J_p(pe) + J_{p+2}(pe)]^2 + \frac{4}{3p^2} [J_p(pe)]^2 \right\}, \quad (4.4)$$

where $J_n(x)$ is the Bessel function. We note that $g(p, 0) = 0$ for $p \neq 2$.

B. optical depth toward the LMC

Let us consider the density profile of the halo. Based upon the number and duration of gravitational microlensing events [1], the optical depth of MACHOs toward the LMC is estimated as

$$\tau^{LMC} \sim 2 \times 10^{-7}. \quad (4.5)$$

While, the optical depth can also be expressed in terms of the number density of MACHOs. Let us assume that the distribution of the number density of MACHOs is spherical symmetric as

$$n(r) = \frac{n_s}{[1 + (r^2/D_a^2)]^\lambda}, \quad (4.6)$$

where r is the distance from the center of our galaxy, n_s is the density of MACHOs at the galactic center, and D_a is the core radius of the distribution [33]. Then the optical depth is given by

$$\tau^{LMC} = \frac{4\pi GM_{BH}}{c^2} \int_0^{D_s} x \left(1 - \frac{x}{D_s}\right) n(r) dx, \quad (4.7)$$

where x is the distance from the earth toward a lens, and D_s is the distance to the LMC from the earth. Here we adopt $D_s = 50$ kpc. In general, r can be expressed by x and the directional cosine, $\cos \theta$, as

$$r^2 = D_0^2 - 2D_0x \cos \theta + x^2, \quad (4.8)$$

where D_0 is the distance from the galactic center to the earth, and we adopt $D_0 = 8.5$ kpc here. When we consider the LMC direction, we adopt $\cos \theta = \eta := 0.153$. If we fix λ and D_a , Eqs. (4.5) and (4.7) determine n_s as

$$n_s = \frac{c^2 \tau^{LMC}}{4\pi GM_{BH} D_a^2} \left[\int_0^{\frac{D_s}{D_a}} dy \frac{y \left(1 - \frac{D_a}{D_s} y\right)}{\left\{1 + \left(\frac{D_0^2}{D_a^2} - 2\frac{D_0}{D_a} \eta y + y^2\right)\right\}^\lambda} \right]^{-1}, \quad (4.9)$$

where the quantity in the square bracket is dimensionless.

C. flux and strain amplitude of the halo background

The contribution to the average flux from the p -th harmonic per unit frequency at ν_{gw} is given by

$$F_\nu^{(p)}(\nu_{gw}) = \int \frac{d^3x}{4\pi d^2} n(r) \int de L^{(p)}(\nu_{gw}, e) f_{\nu,e,t}(\nu_p, e; t_0) \frac{d\nu_p}{d\nu_{gw}} [\text{erg cm}^{-2} \text{ s}^{-1} \text{ Hz}^{-1}], \quad (4.10)$$

where $d = (D_0^2 - 2rD_0 \cos \theta + r^2)^{1/2}$ is the distance between a source and the earth. The probability distribution function $f_{\nu,e,t}(\nu_p, e; t_0)$ is given by Eq. (3.10) and the luminosity from the p -th harmonic, $L^{(p)}(\nu_{gw}, e)$, is given by Eq. (4.2). Defining

$$I := \int \frac{d^3x}{4\pi d^2} n(r), \quad (4.11)$$

the dependence of the flux on the halo model is factorized as

$$F_\nu^{(p)}(\nu_{gw}) = IL_0 \nu_{gw}^{10/3} p^{-13/3} \int_0^1 de f_{\nu,e,t}(\nu_p, e; t_0) g(p, e) [\text{erg cm}^{-2} \text{ s}^{-1} \text{ Hz}^{-1}], \quad (4.12)$$

Using Eq. (4.6) with Eq. (4.9), we find

$$\begin{aligned} I &= \frac{c^2 \tau^{LMC}}{16\pi G M_{BH} D_0} \left[\int_0^\infty y dy \left(\ln \frac{\left(y + \frac{D_0}{D_a}\right)^2}{\left(y - \frac{D_0}{D_a}\right)^2} \right) \frac{1}{(1+y^2)^\lambda} \right] \Big/ \left[\int_0^{\frac{D_s}{D_a}} dy \frac{y \left(1 - \frac{D_a}{D_s} y\right)}{\left[1 + \left(\frac{D_0^2}{D_a^2} - 2\frac{D_0}{D_a} \eta y + y^2\right)\right]^\lambda} \right] \\ &=: \frac{c^2 \tau^{LMC}}{16\pi G M_{BH} D_0} \tilde{I}, \end{aligned} \quad (4.13)$$

where we defined the halo shape factor, \tilde{I} , by the last equality. Note that \tilde{I} is a dimensionless constant which depends only on the shape parameters of the halo (λ and D_a). In Fig. 2, we plot \tilde{I} as a function of the core radius, D_a , for several values of λ . As we can see in Fig. 2, \tilde{I} is about 7 when the halo of our galaxy is isothermal, i.e., when $\lambda = 1$. If the halo is more concentrated to the galactic center, i.e., λ is larger and D_a is smaller, the gravitational wave flux becomes larger.

Collecting the contributions from all harmonics, we obtain the total gravitational wave flux per unit frequency at ν_{gw} as

$$\begin{aligned} F_\nu(\nu_{gw}) &= \sum_{p=1}^{\infty} F_\nu^{(p)}(\nu_{gw}) \\ &= IL_0 \nu_{gw}^{10/3} \sum_{p=1}^{\infty} p^{-13/3} \int_0^1 de f_{\nu,e,t}(\nu_p, e; t_0) g(p, e) [\text{erg cm}^{-2} \text{ s}^{-1} \text{ Hz}^{-1}]. \end{aligned} \quad (4.14)$$

When we evaluate the above expression numerically, we took the summation over p up to $p = 1000$. In Appendix A, we show that the error caused by neglecting higher p harmonics is less than a few percent.

For comparison, it is convenient to translate the gravitational wave flux into the spectral density of the gravitational wave strain amplitude, h_ν , which is calculated by

$$h_\nu^{halo} = \frac{2\sqrt{G}}{c^{3/2}\sqrt{\pi}} \frac{\sqrt{F_\nu}}{\nu_{gw}} = 5.615 \times 10^{-20} \frac{F_\nu^{1/2}}{\nu_{gw}} \quad [\text{Hz}^{-1/2}]. \quad (4.15)$$

In Table I, we list the spectral density $h_\nu^{halo}/\sqrt{\tilde{I}}$ at several frequencies for several BHMACHO masses, M_{BH} , and density parameters, Ωh^2 . Note that $h_\nu^{halo}/\sqrt{\tilde{I}}$ does not depend on the halo shape factor, \tilde{I} . In Fig. 3, the solid line is the spectral density $h_\nu^{halo}/\sqrt{\tilde{I}}$ for $M_{BH} = 0.5M_\odot$ and $\Omega h^2 = 0.1$. We also plot the spectral density obtained by taking the summation up to $p = 10$ in Eq. (4.14) by the long dashed line. We see that the contribution from higher harmonics takes maximum at about 10^{-3} Hz. Even there, the contribution is not so large, and the results coincide with each other within 25%.

D. approximate relations for the halo background

When the condition $e \ll 1$ is satisfied, a good approximation for the halo background can be obtained analytically. Since only the second harmonic contributes to the gravitational wave flux in this case, the total gravitational wave flux in Eq. (4.14) can be approximated by

$$F_\nu(\nu_{gw}) \sim IL_0\nu_{gw}^{10/3}2^{-13/3}f_{\nu,t}(\nu_p; t_0) \quad : e \ll 1, \quad (4.16)$$

where $f_{\nu,t}(\nu_p; t)$ is given by Eq. (3.12). Since a relation $F_\nu(\nu_{gw}) \propto \nu_{gw}^{-1/3}$ can be derived from Eqs. (3.13) and (4.16), the spectral density h_ν^{halo} in Eq. (4.15) satisfies

$$h_\nu \propto \nu_{gw}^{-7/6} \quad : e \ll 1. \quad (4.17)$$

On the other hand, for a fixed gravitational wave frequency, we have $I \propto M_{BH}^{-1}$ from Eq. (4.13), $L_0 \propto M_{BH}^{10/3}$ from Eq. (4.3), and $f_{\nu,t}(\nu_p; t_1) \propto M_{BH}^{-170/111}(\Omega h^2)^{16/37}$ from Eq. (3.14). Then, by using Eqs. (4.15) and (4.16), we find

$$h_\nu^{halo} \propto M_{BH}^{89/222}(\Omega h^2)^{8/37} \quad : e \ll 1. \quad (4.18)$$

As we can see in Table I, these approximate relations hold for $\nu_{gw} \gtrsim 10^{-1}$ Hz, at which almost all binaries that contribute to the halo background are in circular orbits.

In Fig. 3, we plot the approximate spectral density by the dotted line, replacing F_ν in Eq. (4.15) with the approximate one in Eq. (4.16). The dotted line coincides with the solid line quite well at high frequencies, i.e., $\nu_{gw} \gtrsim 10^{-2}$ Hz. This means that almost all binaries that contribute to the gravitational waves at high frequencies are in circular orbits. Conversely, the fact that the spectral density h_ν^{halo} deviates from the approximate value at low frequencies means that binaries with large eccentricity e contribute the gravitational wave flux at low frequencies.

V. COSMOLOGICAL GRAVITATIONAL WAVE BACKGROUND

In the previous section, we studied the gravitational wave background produced by BH-MACHO binaries in the Milky Way halo. In this section, we compute the gravitational wave background produced by extragalactic sources, i.e., the cosmological gravitational wave background, which turns out to dominate the background radiation.

The gravitational wave flux is proportional to the factor, $I = \int d^3x n(r)/4\pi d^2 \sim n(D_0)r$. Strictly speaking, this expression needs some caution because we need to take into account the expansion of the universe when we estimate the cosmological background. However, as a rough estimate, we can use the estimate $I \sim \bar{n}r_{horizon}$ for the cosmological background, where \bar{n} is the mean number density of BHMs and $r_{horizon}$ is the horizon radius. On the other hand, since the mean number density of BHMs in the halo is enhanced by the factor $(r_{galaxy}/r_{halo})^3$, we have $I \sim \bar{n}(r_{galaxy}/r_{halo})^3 r_{halo}$ for the halo background, where r_{galaxy} is the mean separation between galaxies and r_{halo} is the radius of the halo. Then, the ratio of the cosmological background to the halo background is estimated as $(r_{horizon}/r_{galaxy})(r_{halo}/r_{galaxy})^2 \sim (3000\text{Mpc}/1\text{Mpc})(0.05\text{Mpc}/1\text{Mpc})^2 \sim 7.5$. This suggests that the cosmological background can be the same order of the halo background and it cannot be neglected.

A. cosmological model

We assume that the cosmological distribution of BHMACHOs is homogeneous and isotropic. The Hubble equation is

$$H^2 := \left(\frac{\dot{R}}{R} \right)^2 = \frac{8\pi G}{3} \rho - \frac{Kc^2}{R^2}, \quad (5.1)$$

where we assume that the cosmological constant is zero. For simplicity, we assume that the energy density is determined by BHMACHOs and the radiation. The energy densities of BHMACHOs and the radiation at present are denoted by ρ_{BH} and ρ_R , respectively. We refer to the present density parameter of each component as $\Omega_{BH} = \rho_{BH}/\rho_c$ and $\Omega_R = \rho_R/\rho_c$, where $\rho_c = 3H_0^2/8\pi G$ is the critical density and $H_0 = 100h$ km/s/Mpc. Since the energy density of BHMACHOs behaves like that of dust, the total energy density ρ is given by

$$\Omega \frac{\rho}{\rho_0} = \frac{R_0^3}{R^3} \Omega_{BH} + \frac{R_0^4}{R^4} \Omega_R, \quad \Omega = \Omega_{BH} + \Omega_R, \quad (5.2)$$

where quantities with the subscript, 0, represent the present values. Using Eq. (5.1), the relation between the scale factor and the cosmological time, t , is obtained as

$$H_0 dt = \frac{\left(\frac{R}{R_0} \right) d \left(\frac{R}{R_0} \right)}{\left[\Omega_R + \Omega_{BH} \left(\frac{R}{R_0} \right) + (1 - \Omega) \left(\frac{R}{R_0} \right)^2 \right]^{1/2}}, \quad (5.3)$$

where we use Eq. (5.2) and the relation,

$$Kc^2 = R_0^2 H_0^2 (\Omega - 1). \quad (5.4)$$

Since the present temperature of the cosmic microwave background is about 2.75 K, the energy density of the radiation is given by $\rho_R = 4.81 \times 10^{-34} \text{ g cm}^{-3}$. Recalling that the scale factor is normalized such that $R = 1$ at the time of matter-radiation equality, we see that R_0 is given by $1/R_0 = \Omega_R/\Omega_{BH} = 2.56 \times 10^{-4} (\Omega_{BH} h^2)^{-1} \simeq 2.56 \times 10^{-4} (\Omega h^2)^{-1}$.

B. energy density and strain amplitude of the cosmological gravitational wave background

When we consider the cosmological situation, we have to take the redshift into account. Let us consider gravitational waves observed at a frequency ν_{gw} . If they are emitted by a binary at a redshift $1+z = R_0/R$ as the p -th harmonic, the frequency of them at the moment of emission is $\nu_{gw}R_0/R$, and the Keplerian orbital frequency of the binary is given by

$$\nu_p(R) = \frac{R_0}{R} \frac{\nu_{gw}}{p}. \quad (5.5)$$

The gravitational wave luminosity emitted by this binary in the p -th harmonic is evaluated by [31]

$$L^{(p)} \left(\frac{R_0}{R} \nu_{gw}, e \right) = L_0 \left(\frac{R_0}{R} \right)^{10/3} \nu_{gw}^{10/3} p^{-10/3} g(p, e), \quad (5.6)$$

where L_0 is given in Eq. (4.3). Then, the gravitational wave luminosity per unit logarithmic frequency at ν_{gw} per BHMACHO is given by

$$\begin{aligned} \mathcal{L}_{GW}(\nu_{gw}; t) &= \sum_{p=1}^{\infty} \int de L^{(p)} \left(\frac{R_0}{R} \nu_{gw}, e \right) f_{\nu, e, t}(\nu_p, e; t) \nu_{gw} \frac{d\nu_p}{d\nu_{gw}} \\ &= L_0 \nu_{gw}^{13/3} \left(\frac{R_0}{R} \right)^{13/3} \sum_{p=0}^{\infty} p^{-13/3} \int de f_{\nu, e, t}(\nu_p, e; t) g(p, e) \quad [\text{erg s}^{-1}]. \end{aligned} \quad (5.7)$$

In order to characterize the spectrum of stochastic gravitational waves, we often use $\Omega_{GW}(\nu_{gw})$, the ratio of the energy density of the gravitational waves per unit logarithmic frequency to the critical density [34]. To evaluate $\Omega_{GW}(\nu_{gw})$, we use the fact that the gravitational wave energy existing in a unit comoving volume is equal to the red-shifted total gravitational wave energy that is emitted per unit comoving volume until now. The gravitational wave energy per unit logarithmic frequency in a unit comoving volume is given by $\rho_c c^2 \Omega_{GW}(\nu_{gw}) R_0^3$. On the other hand, the latter quantity can be evaluated as follows. The comoving number density of BHMACHO is given by $(1/\bar{x})^3$, where \bar{x} is the mean separation at the time of matter-radiation equality given in Eq. (2.2). Then, the red-shifted total

gravitational wave energy that is emitted per unit comoving volume per unit logarithmic frequency during $t \sim t + dt$ is given by $\mathcal{L}_{GW}(\nu_{gw}; t) (1/\bar{x})^3 dt$. Integrating this expression multiplied by the red-shift factor (R/R_0) , we obtain the quantity that is to be equated with $\rho_c c^2 \Omega_{GW}(\nu_{gw}) R_0^3$.

From the above consideration, we obtain

$$\begin{aligned} \Omega_{GW}(\nu_{gw}) &= \frac{1}{\rho_c c^2} \int_{t_f}^{t_0} dt \left(\frac{R}{R_0} \right) \left(\frac{1}{\bar{x} R_0} \right)^3 \mathcal{L}_{GW}(\nu_{gw}; t) \\ &= \int_{R_m/R_0}^1 d \left(\frac{R}{R_0} \right) \frac{\mathcal{L}_{GW}(\nu_{gw}; t(R))}{\rho_c c^2 H_0} \frac{\left(\frac{R}{R_0} \right)^5 \left(\frac{1}{\bar{x} R} \right)^3}{\left[\Omega_R + \Omega_{BH} \left(\frac{R}{R_0} \right) + (1 - \Omega) \left(\frac{R}{R_0} \right)^2 \right]^{1/2}}. \end{aligned} \quad (5.8)$$

The relation between t and R is given by Eq. (5.3) and the binary formation time, t_f , is the time at which R equals to R_m given in Eq. (2.3). Hereafter, we set $h = 0.8$, when quantities with $\rho_c c^2$ or H_0 are evaluated numerically. In the case of $h = 0.8$ and $\Omega h^2 = 0.1$, the present age of the universe, t_0 , is about 1.06×10^{10} yr.

In Fig. 4, we plot $d\Omega_{GW}(\nu_{gw})/d(\ln R)$, which is the integrand of the last line of Eq. (5.8), as a function of the scale factor R/R_0 by the solid lines for $M_{BH} = 0.5M_\odot$ and $\Omega_{BH}h^2 = 0.1$ at several frequencies. When we evaluate $\mathcal{L}_{GW}(\nu_{gw}; t)$ given in Eq. (5.7) numerically, we perform the summation up to $p = 10$. The computational time does not allow us to sum up higher harmonics. Since the power index of $d\Omega_{GW}(\nu_{gw})/d(\ln R)$ with respect to R is larger than 0, the contribution to the energy density from binaries at higher redshift is smaller. Therefore, we perform the integration in Eq. (5.8) from $R/R_0 = 1/R_0$ (not R_m/R_0) to $R/R_0 = 1$ to evaluate the energy density of the cosmological background numerically.²

In Fig. 5, we plot the density parameter of the cosmological gravitational wave back-

²Note that, when the redshift is too high, the orbital frequency in Eq. (5.5) may become larger than ~ 1000 Hz. Since such binaries are not allowed to exist for black hole binaries with $M_{BH} \sim M_\odot$, the summation over them should be eliminated. However, such a complication is unnecessary as long as we consider $\nu_{gw} \lesssim 10^{-1}$ Hz, for which at $R > 1$ the orbital frequency is less than ~ 1000 Hz.

ground per unit logarithmic frequency, $\Omega_{GW}(\nu_{gw})$, for $M_{BH} = 0.5M_{\odot}$ and $\Omega h^2 = 0.1$. We again take the summation until $p = 10$ in Eq. (5.7). However, as we have seen at the end of Section. IV C, the contribution from higher harmonics is not so large. For example, we calculated the density parameter of the cosmological gravitational wave background per unit logarithmic frequency at $\nu_{gw} = 10^{-7}$ Hz for $M_{BH} = 0.5M_{\odot}$ and $\Omega h^2 = 0.1$. When the summation is taken until $p = 10$, we have $\Omega_{GW}(\nu_{gw}) = 2.7 \times 10^{-20}$. While, when the summation is taken until $p = 1000$, we have $\Omega_{GW}(\nu_{gw}) = 3.2 \times 10^{-20}$.

The spectral density of the cosmological gravitational wave strain amplitude is given by

$$h_{\nu}^{cos} = 5.615 \times 10^{-20} \frac{\sqrt{\rho_c c^3 \Omega_{GW}(\nu_{gw})}}{\nu_{gw}^{3/2}} \quad [\text{Hz}^{-1/2}]. \quad (5.9)$$

Note that the flux from the cosmological BHMACHO binaries per unit frequency at ν_{gw} is $\rho_c c^3 \Omega_{GW}(\nu_{gw})/\nu_{gw}$, which corresponds to $F_{\nu}(\nu_{gw})$ in Eq. (4.14) for the halo background. In Table II, we list the spectral density, h_{ν}^{cos} , at several frequencies for several BHMACHO masses, M_{BH} , and the density parameters, Ωh^2 . We present the figure of h_{ν}^{cos} in Sec.VI.

C. approximate relations for the cosmological background

When the condition $e \ll 1$ is satisfied, Eq. (5.7) can be approximated by

$$\mathcal{L}_{GW}(\nu_{gw}; t) \sim L_0 \nu_{gw}^{13/3} \left(\frac{R_0}{R} \right)^{13/3} 2^{-13/3} f_{\nu,t}(\nu_p; t) \quad : e \ll 1, \quad (5.10)$$

where $f_{\nu,t}(\nu_p; t)$ is given in Eq. (3.12). When Ω_{BH} is of order unity, R is approximately proportional to $t^{2/3}$ during the matter dominant era. For a fixed gravitational wave frequency ν_{gw} , we can extract R -dependence from Eq. (3.12) as $f_{\nu,R}(\nu_p; R) \propto t^{-34/37} \nu_p(R)^{-11/3} \propto R^{254/111}$, where we used the relation $a \propto \nu_p(R)^{-2/3} \propto R^{2/3}$ that follows from Eqs. (3.9) and (5.5). Hence, from Eq. (5.10) we can see that $\mathcal{L}_{GW}(\nu_{gw}; t) \propto R^{-227/111}$ is approximately satisfied. Since $[\Omega_R + \Omega_{BH}(R/R_0) + (1 - \Omega)(R/R_0)^2]^{-1/2}$ can be approximated by $\Omega_{BH}^{-1/2}(R/R_0)^{-1/2}$ during the matter dominant era, we find that the integrand in Eq. (5.8) is approximately proportional to $R^{-121/222}$. In Fig. 4, we also plot the approximation of

$d\Omega_{GW}(\nu_{gw})/d(\ln R)$ by the dotted lines, replacing the luminosity \mathcal{L}_{GW} in Eq. (5.7) with the approximation given in Eq. (5.10). The solid lines coincide with the dotted ones well for high frequencies. At high redshift almost all binaries that contribute to the gravitational wave flux at all relevant frequencies are in circular orbits, as is seen from the agreement of the solid and the dotted lines.

When the approximation (5.10) is valid, with the aid of Eq. (3.13), it implies $\mathcal{L}_{GW}(\nu_{gw}; t) \propto \nu_{gw}^{2/3}$. Thus we find $\Omega_{GW}(\nu_{gw}) \propto \nu_{gw}^{2/3}$, and hence

$$h_{\nu}^{cos} \propto \nu_{gw}^{-7/6} \quad : e \ll 1. \quad (5.11)$$

This dependence on ν_{gw} is the same as that obtained in the halo background case in Eq. (4.17). For fixed ν_{gw} and t , we have approximate relations $(1/\bar{x})^3 \propto M_{BH}^{-1}$ from Eq. (2.2), $L_0 \propto M_{BH}^{10/3}$ from Eq. (4.3), and $f_{\nu,R}(\nu_p; R) \propto M_{BH}^{-170/111}$ from Eq. (3.14). Therefore, $\Omega_{GW}(\nu_{gw}) \propto M_{BH}^{89/111}$ is derived from Eqs. (5.8) and (5.10), and hence we find there is an approximate relation

$$h_{\nu}^{cos} \propto M_{BH}^{89/222} \quad : e \ll 1. \quad (5.12)$$

As we can see in Table. II, this relation is satisfied for $\nu_{gw} \gtrsim 10^{-1}$ Hz, at which almost all binaries that contribute to the cosmological background are in circular orbits. The dependence of the spectral density, h_{ν}^{cos} , on the density parameter Ωh^2 cannot be derived so easily in an analytic method.

D. observational limit

There are several observational constraints on the cosmological gravitational wave background. These constraints come from the millisecond pulsar timing, quasar proper motions, the standard model of big bang nucleosynthesis, and so on. In this section, we study whether or not the cosmological gravitational wave background produced by BHMACHO binaries satisfies these constraints.

At the time of the nucleosynthesis, the effective number of neutrino species is restricted to be less than three, to be consistent with the observations of He, D, and Li [35]. If the effective number of neutrino species were larger than three, the expansion rate at the time of the nucleosynthesis would become larger and the predicted abundance of He, D and Li would differ. Since the gravitational wave background contributes to the energy density in the same way as neutrinos, the constraint on the effective number of neutrino species restricts the energy density of the cosmological gravitational wave background within that of one massless degree of freedom in thermal equilibrium. If the cosmological gravitational wave background already exists at the time of the big bang nucleosynthesis, $\Omega_{GW}(\nu_{gw})$ is restricted approximately by

$$\int d(\ln \nu_{gw}) \Omega_{GW}(\nu_{gw}) h^2 \lesssim 10^{-5}. \quad (5.13)$$

Here, we should note that gravitational wave background produced after the nucleosynthesis is not restricted by Eq. (5.13) at all.

Observations of stable millisecond pulsars provide a constraint on the energy density of the gravitational waves [36,37]. Gravitational waves deform the metric perturbing the observed pulsar frequency. Therefore, the fluctuations in pulse arrival times are used to constrain the gravitational waves. Pulsar timing residuals are most sensitive to gravitational waves at frequencies around $1/T$, where T is the total data span. Observations of PSR B 1855+09 yield an upper limit,

$$\Omega_{GW}(\nu_{gw}) h^2 < 1.0 \times 10^{-8} \quad (95\% \text{ confidence}), \quad (5.14)$$

at $\nu_{gw} \sim 4.4 \times 10^{-9} \text{ Hz}$.

After taking into account the energy carried away by gravitational waves and the effects of Galactocentric acceleration, orbital periods of binary pulsars are sensitive to gravitational waves with periods as great as the light-travel time from the pulsar. Current limits from such data are [37]

$$\Omega_{GW}(\nu_{gw}) h^2 < 0.04 \quad (95\% \text{ confidence}), \quad (5.15)$$

in the range $10^{-11}\text{Hz} \lesssim \nu_{gw} \lesssim 10^{-9}\text{Hz}$, and

$$\Omega_{GW}(\nu_{gw})h^2 < 0.5 \quad (95\% \text{ confidence}), \quad (5.16)$$

in the range $10^{-12}\text{Hz} \lesssim \nu_{gw} \lesssim 10^{-11}\text{Hz}$.

Background gravitational waves randomly scatter photons from distant quasars on its way to the earth. This may cause quasar proper motions. Using measurements of the proper motions of quasars, upper limits on the energy density of gravitational waves with periods longer than the time span of observations is obtained [38] as

$$\Omega_{GW}(\nu_{gw})h^2 \lesssim 0.11 \quad (95\% \text{ confidence}), \quad (5.17)$$

in the range $\nu_{gw} < 2 \times 10^{-9} \text{ Hz}$.

However, these limits are not enough to reject the existence of BHMACHOs. As we can see in Fig. 5, the cosmological gravitational wave background produced by BHMACHO binaries, $\Omega_{GW}(\nu_{gw})$, is less than these limits at $10^{-9} \text{ Hz} < \nu_{gw} < 10^{-1} \text{ Hz}$. At higher frequencies $\nu_{gw} > 10^{-1} \text{ Hz}$, $\Omega_{GW}(\nu_{gw})$ continues to grow as $\Omega_{GW}(\nu_{gw}) \propto \nu_{gw}^{2/3}$ till $\nu_{gw} \sim 10^3 \text{ Hz}$. However, the constraint in Eq. (5.13) is still satisfied even at frequencies $\nu_{gw} \sim 10^3 \text{ Hz}$. Furthermore, since almost all background at these frequencies is produced after the nucleosynthesis, Eq. (5.13) is not a real constraint for the existence of BHMACHOs. At $\nu_{gw} < 10^{-9} \text{ Hz}$, $\Omega_{GW}(\nu_{gw})$ will continue to fall. Therefore, all constraints (5.15), (5.16) and (5.17) will be satisfied.

VI. OTHER BACKGROUND NOISES

The gravitational wave strain amplitude h_ν due to various galactic binary systems is obtained in Ref. [39] (see also [40,41]). Among these binary systems, the background due to Close White Dwarf Binaries (CWDBs) is dominant at relevant frequencies, $10^{-4}\text{Hz} \lesssim \nu_{gw} \lesssim 10^{-1}\text{Hz}$. We obtain the spectral density due to CWDBs, h_ν^{WD} , from Table. 7 in Ref. [39], where the space density of CWDBs is assumed to take the maximal theoretical value in the calculations of Webbink [42].

In addition to this background, there are instrumental noises. The instrumental noises can be classified into two kinds, i.e., the optical-path noise and the acceleration noise. The optical-path noise, which includes the shot noise, beam pointing instabilities and so on, dominates at high frequencies and is estimated as [43,34]

$$h_{\nu}^{opt} = \frac{4 \times 10^{-11} \text{m}/\sqrt{\text{Hz}}}{2L} \times \sqrt{1 + (2\pi L \nu_{gw}/c)^2} \simeq 4 \times 10^{-21} \sqrt{1 + 1.097 \left(\frac{\nu_{gw}}{10^{-2} \text{Hz}} \right)^2} \quad [\text{Hz}^{-1/2}], \quad (6.1)$$

where we adopted $2L = 10^{10}$ m. We include the last factor $\sqrt{1 + (2\pi L \nu_{gw}/c)^2}$ considering the fact that the sensitivity decreases when the wave period is shorter than the round-trip light travel time in one of LISA's arms. The acceleration noise, which includes the thermal distortion of spacecraft, the gravity noise due to spacecraft displacement and so on, dominates at low frequencies and is estimated as [43]

$$h_{\nu}^{acc} = \frac{6 \times 10^{-15} (\nu_{gw}/10^{-4} \text{Hz})^{-1/3} \text{ms}^{-2}/\sqrt{\text{Hz}}}{2L(2\pi\nu_{gw})^2} \simeq 1.52 \times 10^{-18} \left(\frac{\nu_{gw}}{10^{-4} \text{Hz}} \right)^{-7/3} \quad [\text{Hz}^{-1/2}]. \quad (6.2)$$

In Fig. 6, setting $M_{BH} = 0.5M_{\odot}$ and $\Omega h^2 = 0.1$, we summarize the spectral density for the cosmological background, h_{ν}^{cos} , in Eq. (5.9) and that for the halo background, h_{ν}^{halo} , in Eq. (4.15) together with the spectral density for CWDBs, h_{ν}^{WD} , and that due to the two kinds of instrumental noises, h_{ν}^{opt} and h_{ν}^{acc} . When we plot the halo background case, we assumed an isothermal halo. As we can see from Fig. 6, the cosmological background dominates the halo background for an isothermal halo with this choice of model parameters. Since the dependence of the cosmological background on Ωh^2 is different from that of the halo background, which we can see in Table I and Table II, the halo background dominates the cosmological background when the density parameter of BHMACOs is very small. However, since such a situation is less interesting for us, we neglect the halo background hereafter. Of course, if the halo is more concentrated, i.e., λ is larger and R_a is smaller, the halo background can dominate the cosmological background, as we can see from Fig. 2.

At first glance, the spectral density due to CWDBs, h_ν^{WD} , dominates the cosmological background due to BHMACHOs, h_ν^{cos} . However, the cosmological background due to BHMACHOs, h_ν^{cos} , can be more important. This is because the confusion noise level for detection of individual sources also depends on the number of noise sources in a frequency resolution bin. At lower frequencies many galactic CWDBs exist in a frequency resolution bin, while the expected number at higher frequencies becomes less than one. Hence the confusion noise level determined by CWDBs decreases suddenly at a transition frequency $\nu_{gw} \sim 10^{-2.5}$ Hz [44]. Therefore, as for the confusion noise level, the cosmological background produced by BHMACHO binaries dominates the background due to CWDBs above the transition frequency.

VII. INDIVIDUAL SOURCE

A. expected number

Let us consider the expected number of observable individual sources. The frequency resolution is determined by the observing time T [45,34]. Here we assume that the frequency resolution is given by

$$\Delta\nu = \frac{1}{T}, \quad (7.1)$$

with $T \sim 1$ yr. For the noise amplitude, h_ν , the threshold amplitude of gravitational waves from individual sources is given by,

$$h^{th} = 5h_\nu\Delta\nu^{1/2}, \quad (7.2)$$

where we set the signal-to-noise ratio (SNR) as 5. ³

³Here we do not consider a reduction factor due to the antenna pattern of an interferometer. Hence, we overestimate the number of individual sources in the following discussion. A traditional

The amplitude of gravitational wave at ν_{gw} from a binary with e , p and the distance from the earth, d , is given by

$$h = \frac{2\sqrt{G}}{c^{3/2}\sqrt{\pi}} \frac{\sqrt{F_i}}{\nu_{gw}}, \quad F_i = \frac{L^{(p)}(\nu_{gw}, e)}{4\pi d^2}, \quad (7.3)$$

where $L^{(p)}(\nu_{gw}, e)$ is given by Eq. (4.2). Then, the requirement that the signal exceeds the threshold, $h > h^{th}$, determines the maximum distance to individually observable sources,

$$D_{max}^{(p)}(\nu_{gw}, e) = \frac{\sqrt{G}}{\pi c^{3/2} h^{th}} \sqrt{L_0 g(p, e)} \nu_{gw}^{2/3} p^{-5/3}, \quad (7.4)$$

where L_0 is given by Eq. (4.3). Then the expected number of individual sources per unit logarithmic frequency in the p -th harmonic is given by

$$N^{(p)}(\nu_{gw}) = \int de \mathcal{N}^{(p)}(\nu_{gw}, e) \nu_{gw} \frac{d\nu_p}{d\nu_{gw}} f_{\nu, e, t}(\nu_p, e; t_0) = \int de \mathcal{N}^{(p)}(\nu_{gw}, e) \frac{\nu_{gw}}{p} f_{\nu, e, t}(\nu_p, e; t_0), \quad (7.5)$$

and

$$\mathcal{N}^{(p)}(\nu_{gw}, e) = \int_{d < D_{max}^{(p)}(\nu_{gw}, e)} n(r) d^3x, \quad (7.6)$$

where $f_{\nu, e, t}(\nu_p, e; t_0)$ and $n(r)$ are given in Eqs. (3.10) and (4.6), respectively. The expected number of individual sources per unit logarithmic frequency is given by

$$N(\nu_{gw}) = \sum_{p=1}^{\infty} N^{(p)}(\nu_{gw}). \quad (7.7)$$

The total expected number in the range of $\nu_1 < \nu_{gw} < \nu_2$ is

$$N^{tot} = \int_{\ln \nu_1}^{\ln \nu_2} N(\nu_{gw}) d(\ln \nu_{gw}). \quad (7.8)$$

When $D_{max}^{(p)}(\nu_{gw}, e)$ is much smaller than the distance to the center of our galaxy from us, D_0 , under the assumption of the uniform density we can approximate Eq. (7.6) as

way to take this factor into account is to adopt the root-mean-square value of the signal averaged over the entire sky, which implies that the reduction factor is $\sqrt{5}$ [34,43].

$$\mathcal{N}^{(p)}(\nu_{gw}) = \frac{4\pi n(D_0)}{3} [D_{max}^{(p)}(\nu_{gw}, e)]^3 = K \frac{c^2 \tau^{LMC}}{3GM_{BH}D_0^2} [D_{max}^{(p)}(\nu_{gw}, e)]^3 \quad : D_{max}^{(p)}(\nu_{gw}, e) \ll D_0, \quad (7.9)$$

where

$$K = \frac{D_0^2/D_a^2}{[1 + (D_0^2/D_a^2)]^\lambda} \left[\int_0^{\frac{D_s}{D_a}} dy \frac{y \left(1 - \frac{D_a}{D_s}y\right)}{\left[1 + \left(\frac{D_0^2}{D_a^2} - 2\frac{D_0}{D_a}\eta y + y^2\right)\right]^\lambda} \right]^{-1} \quad (7.10)$$

is a factor obtained from Eqs. (4.6) and (4.9) which depends only on the shape of our galaxy. In Fig. 7, we plot K as a function of the core radius, R_a , in units of kpc for $\lambda = 1, 1.5$ and 2. K is about 0.8 when $\lambda \simeq 1$.

When such an approximation is not valid, we have to integrate Eq. (7.6). When λ is integer, however, we can integrate Eq. (7.6) analytically. Evaluating the integrals

$$\begin{aligned} \mathcal{N}^{(p)}(\nu_{gw}, e) &= \int_0^{D_{max}^{(p)}(\nu_{gw}, e) - D_0} dr 4\pi r^2 n(r) \\ &+ \int_{D_{max}^{(p)}(\nu_{gw}, e) - D_0}^{D_{max}^{(p)}(\nu_{gw}, e) + D_0} dr 2\pi r^2 n(r) \left[1 - \frac{D_0^2 + r^2 - (D_{max}^{(p)}(\nu_{gw}, e))^2}{2rD_0} \right], \end{aligned} \quad (7.11)$$

for $D_{max}^{(p)}(\nu_{gw}, e) > D_0$, and

$$\mathcal{N}^{(p)}(\nu_{gw}, e) = \int_{D_0 - D_{max}^{(p)}(\nu_{gw}, e)}^{D_0 + D_{max}^{(p)}(\nu_{gw}, e)} dr 2\pi r^2 n(r) \left[1 - \frac{D_0^2 + r^2 - (D_{max}^{(p)}(\nu_{gw}, e))^2}{2rD_0} \right], \quad (7.12)$$

for $D_{max}^{(p)}(\nu_{gw}, e) < D_0$, we find both expressions (7.11) and (7.12) give the same results,

$$\begin{aligned} \lambda = 1 : \quad \mathcal{N}^{(p)}(\nu_{gw}, e) &= \frac{4\pi}{3} [D_{max}^{(p)}(\nu_{gw}, e)]^3 n_s \left\{ -\frac{3}{2} r_a^4 [I_A(1 + r_0) + I_A(1 - r_0)] + \frac{3}{2} r_a^2 \right. \\ &\quad \left. + \frac{3r_a^2}{8r_0} (1 - r_0^2 + r_a^2) \ln \left[\frac{(1 + r_0)^2 + r_a^2}{(1 - r_0)^2 + r_a^2} \right] \right\}, \end{aligned} \quad (7.13)$$

$$\begin{aligned} \lambda = 2 : \quad \mathcal{N}^{(p)}(\nu_{gw}, e) &= \frac{4\pi}{3} [D_{max}^{(p)}(\nu_{gw}, e)]^3 n_s \left\{ \frac{3}{4} r_a^4 [I_A(1 + r_0) + I_A(1 - r_0)] \right. \\ &\quad \left. - \frac{3r_a^4}{8r_0} \ln \left[\frac{(1 + r_0)^2 + r_a^2}{(1 - r_0)^2 + r_a^2} \right] \right\}, \end{aligned} \quad (7.14)$$

where

$$r_a = \frac{D_a}{D_{max}^{(p)}(\nu_{gw}, e)}, \quad r_0 = \frac{D_0}{D_{max}^{(p)}(\nu_{gw}, e)}, \quad I_A(x) = \frac{1}{r_a} \arctan \left(\frac{x}{r_a} \right). \quad (7.15)$$

When $D_{max}^{(p)}(\nu_{gw}, e)$ is much larger than the core radius, D_a , and the distance between the center of our galaxy and us, D_0 , Eqs. (7.13) and (7.14) can be approximated as

$$\lambda = 1 : \quad \mathcal{N}^{(p)}(\nu_{gw}, e) = 4\pi D_a^2 D_{max}^{(p)}(\nu_{gw}, e) n_s \quad : D_{max}^{(p)}(\nu_{gw}, e) \gg D_0, D_a, \quad (7.16)$$

$$\lambda = 2 : \quad \mathcal{N}^{(p)}(\nu_{gw}, e) = \pi^2 D_a^3 n_s \quad : D_{max}^{(p)}(\nu_{gw}, e) \gg D_0, D_a. \quad (7.17)$$

B. the case when the confusion limit is determined by BHMACHOs and instrumental noises

Since neither the abundance of halo CWDBs nor that of cosmological BHMACHOs has not been established, we do not know which background determines the confusion limit of individual sources. In this subsection, we assume that BHMACHOs dominate the energy density of the present universe, and they also determine the amplitude of the gravitational wave background. As we have seen in Sec.VI, under this assumption it is natural to think that the cosmological background dominates the halo background. Then the total noise amplitude is determined by

$$h_\nu^{tot} = \sqrt{(h_\nu^{cos})^2 + (h_\nu^{opt})^2 + (h_\nu^{acc})^2}, \quad (7.18)$$

where h_ν^{cos} , h_ν^{opt} and h_ν^{acc} are given in Eqs. (5.9), (6.1) and (6.2), respectively.

In Fig. 8, we plot the expected number of individual sources in each harmonic $N^{(p)}(\nu_{gw})$ for $p = 1, 2, 3, 4$ and 5 . The solid lines are the expected number for $\lambda = 1$, $D_a = 5$ kpc, $M_{BH} = 0.5M_\odot$ and $\Omega h^2 = 0.1$. As we can see in Fig. 8, the second harmonic at high frequencies is prominent. Therefore, the estimate of the total number does not affected by errors in the estimate of the noise level at low frequencies so much, which errors are partly caused by truncating the summation at $p = 10$ in Eq. (5.7). In Fig. 9, we plot the maximum distance of observable individual source defined by $D_{max}^{(p)}(\nu_{gw}, e_{peak})$ for $p = 1, 2, 3, 4$ and 5 , where e_{peak} is the eccentricity at which the distribution function $f_{\nu, e, t}(\nu_p, e; t_0)$ is maximum. As we can see in Fig. 9, the maximum distance $D_{max}^{(p)}(\nu_{gw}, e_{peak})$ extends beyond $\sim 10^2$

kpc at high frequencies. This means that almost all halo BHMACHO binaries radiating gravitational waves at these frequencies can be observed as individual sources. In Fig. 10, we plot the total expected number of the individual sources per logarithmic frequency, $N(\nu_{gw})$, in Eq. (7.7) with the solid line. The dotted line is the expected number using Eq. (7.9) with $K = 0.8$, which is valid for $D_{max}^{(p)}(\nu_{gw}, e) \ll D_0$. The dashed line is the expected number using Eq. (7.16), which is valid for $D_{max}^{(p)}(\nu_{gw}, e) \gg D_0, D_a$. From this figure, we can see that Eqs. (7.9) and (7.16) are good approximations for $D_{max}^{(p)}(\nu_{gw}, e) \ll D_0$ and for $D_{max}^{(p)}(\nu_{gw}, e) \gg D_0$, respectively. The total expected number, N^{tot} , in Eq. (7.8) in the range of $10^{-4}\text{Hz} < \nu_{gw} < 10^{-1}\text{Hz}$ is about 792 for $\lambda = 1$, $D_a = 5$ kpc, $M_{BH} = 0.5M_\odot$ and $\Omega h^2 = 0.1$.

Now we show N^{tot} is approximately proportional to $M_{BH}^{-281/407}$ for $M_{BH} \sim M_\odot$. Since the second harmonic at high frequencies almost completely determines N^{tot} , it is sufficient to consider only $p = 2$ and $e \ll 1$ case. In this case, from Eq. (7.4) with Eqs. (4.3), (5.11) and (5.12), we find the maximum distance $D_{max}^{(2)}(\nu_{gw}, 0)$ is proportional to $\nu_{gw}^{11/6} M_{BH}^{281/222}$. The expected number per unit logarithmic frequency, $N(\nu_{gw})$, has a maximum value when $D_{max}^{(2)}(\nu_{gw}, 0) \sim D_0$, as we can see in Fig. 9 and Fig. 10. Therefore, the frequency ν_{gw} at which $N(\nu_{gw})$ has a maximum value is proportional to $M_{BH}^{-281/407}$. At this frequency, we can use the expression for $\mathcal{N}^{(2)}(\nu_{gw}, 0)$ given in Eq. (7.16), which turns out to be proportional to M_{BH}^{-1} with the aid of Eq. (4.9). On the other hand, using Eqs. (3.13) and (3.14), we see $\nu_{gw} \int def_{\nu, e, t}(\nu_p, e; t_0)$ is approximately proportional to $\nu_{gw} f_{\nu, e}(\nu_p; t_0) \propto \nu_{gw}^{-8/3} M_{BH}^{-170/111} \propto M_{BH}^{126/407}$. Thus, we obtain $N^{(2)}(\nu_{gw}) \propto M^{-281/407}$ from Eq. (7.5). Since the total expected number is approximately determined by the maximum value of $N^{(2)}(\nu_{gw})$, the relation $N^{tot} \propto M_{BH}^{-281/407}$ is obtained. Here we note that N^{tot} does not strongly depend on M_{BH} for $M_{BH} \sim M_\odot$.⁴

⁴This dependence cannot hold for extreme values of M_{BH} .

C. the case when the confusion limit is determined by CWDBs and instrumental noises

In this section we assume that gravitational wave background due to CWDBs and the instrumental noises determine the confusion limit. As noted at the end of Sec.VI, the confusion noise level due to CWDBs decreases suddenly at frequency $\nu_{gw} \sim 10^{-2.5}$ Hz. Thus, even if the confusion noise level is determined by CWDBs at low frequencies, the role of CWDBs is replaced with BHMACHOs at high frequencies. Therefore, the background due to BHMACHOs must be simultaneously taken into account. However, for simplicity, we ignore the background due to BHMACHOs in this subsection. Instead, we neglect the sudden decrease in the confusion noise level due to CWDBs, and hence the estimate given in this subsection will provide a lower bound for the total expected number.

Now, the total noise amplitude is determined by

$$h_\nu^{tot} = \sqrt{(h_\nu^{WD})^2 + (h_\nu^{opt})^2 + (h_\nu^{acc})^2}, \quad (7.19)$$

where h_ν^{WD} is taken from Table 7 in Ref. [39] and we use the linear interpolation.

As before, since the expected number in the second harmonic at high frequencies is prominent, the total expected number is almost insensitive to the noise uncertainty at low frequencies. In Fig. 11, we plot the maximum distance $D_{max}^{(p)}(\nu_{gw}, e_{peak})$ for $p = 1, 2, 3, 4$ and 5. In Fig. 12, we plot the total expected number of the individual sources per unit logarithmic frequency, $N(\nu_{gw})$, in Eq. (7.7). For comparison, with the dotted line, we plot again the total expected number per unit logarithmic frequency, $N(\nu_{gw})$, when the background due to BHMACHOs is dominant. It is the same plot that is presented by the solid line in Fig. 10. The total expected number N^{tot} in Eq. (7.8) in the range of $10^{-4}\text{Hz} < \nu_{gw} < 10^{-1}\text{Hz}$ is about 329.

VIII. SUMMARY

In this paper, we have investigated low frequency gravitational waves emitted by BHMACHO binaries. We have evaluated the gravitational wave background produced by BHMACHO binaries in the Milky Way halo. We have also evaluated the cosmological gravitational wave background produced by the extragalactic BHMACHO binaries, which is larger than the halo background when we assume that the density profile of our halo is isothermal. The root-mean-square strain amplitude of the gravitational wave background due to CWDBs is possibly larger than that due to the extragalactic BHMACHO binaries. However, once the number of CWDBs per frequency resolution bin is taken into account, the cosmological gravitational wave background due to extragalactic BHMACHO binaries will determine the confusion limit for the detection of individual sources at $\nu_{gw} \gtrsim 10^{-2.5}$ Hz. We have found that the cosmological gravitational wave background produced by BHMACHO binaries is well below the existing observational limits obtained from the pulsar timing, the quasar proper motions, the big bang nucleosynthesis and so on. We have found that one year observation by LISA will be able to reveal at least several hundreds of BHMACHO binaries whose gravitational wave amplitudes exceed the confusion limit when we require the *SNR* to be greater than 5 for detection. If the confusion limit is determined by the noises due to extragalactic BHMACHO binaries and instruments, the expected number of observable individual BHMACHO binaries will be about eight hundreds. This suggests that LISA will be able to clarify whether MACHOs are primordial black holes or not, together with the results of LIGO-VIRGO-TAMA-GEO network.

At frequencies above $\sim 10^{-2.23}(T/1\text{yr})^{-6/11}(M_{BH}/0.5M_{\odot})^{-5/11}$, LISA can measure distances to BHMACHO binaries since binaries significantly change their orbital frequencies through gravitational wave emission within the observation time T [43]. Moreover, the LISA's angular resolution is roughly 10^{-3} steradians (equivalently, 3 square degrees) at frequencies $\nu_{gw} \sim 10^{-2}$ Hz for $SNR = 5$ [46]. Therefore, it will be possible to draw a map of the distribution of BHMACHO binaries. Recall that the BHMACHO binaries trace the

mass distribution of the Milky Way halo. Then, if MACHOs are black holes, it may be possible to obtain the mass distribution of our galaxy! Note that the expected number of BHMACHO binaries is large enough to obtain a precise map, and the maximum distance to observable individual sources, $\sim 10^2$ kpc, is sufficiently large as shown in Fig. 9 and Fig. 11.

There may be other observational signals of BHMACHOs except for gravitational waves from BHMACHO binaries which are formed in the early universe. For example, we may be able to detect gravitational waves from BHMACHOs orbiting a massive black hole in a galactic nuclei [47–49], though the event rate is uncertain. Moreover, massive black holes in galactic nuclei may be formed from the BHMACHOs through their merging process [50]. Gravitational waves from their mergers may be detected by LISA, though the event rate is also uncertain. It is a future problem to obtain a reliable estimate of the event rate for such events.

There are two microlensing events toward the LMC and the Small Magellanic Cloud [51–54]. In both events, the lens objects are not likely in our halo. However, the fraction of BHMACHOs that are in binaries with $a \sim 2 \times 10^{14}$ cm and $M_{BH} = 0.5M_{\odot}$ is found to be $\sim 0.45\%$ for $\Omega h^2 = 0.1$, taking into account the evolution of the BHMACHO binaries. (In Ref. [27,28], we did not take the evolution into account). Therefore, no detection of halo binary lens events does not conflict with the BHMACHO scenario.

ACKNOWLEDGMENTS

We would like to thank professor H. Sato for continuous encouragement and useful discussions. We are also grateful to K. Nakao, R. Nishi, T. Chiba and K. Taniguchi for useful discussions. This work was supported in part by Grant-in-Aid of Scientific Research of the Ministry of Education, Culture, Science and Sports, 09640351.

APPENDIX A: THE CONTRIBUTION FROM HIGH p -TH HARMONICS

In this section, we investigate how large the contribution from high p -th harmonics to the gravitational wave flux in Eq. (4.14). As we can see in Eq. (4.14), the gravitational wave flux from BHMACHO binaries in the Milky Way halo per unit frequency at ν_{gw} is given by

$$F_\nu(\nu_{gw}) = IL_0\nu_{gw}^{10/3} \sum_{p=1}^{\infty} \mathcal{F}(p), \quad (\text{A1})$$

where

$$\mathcal{F}(p) = p^{-13/3} \int_0^1 de f_{\nu,e,t}(\nu_p, e; t_0) g(p, e). \quad (\text{A2})$$

For a fixed large $p \gtrsim 100$, $g(p, e)$ has a peak at $e \sim 1$, and the maximum of $g(p, e)$ is about several times of $g(p, 1)$.⁵ Therefore, for a fixed large $p \gtrsim 100$, $g(p, e)$ has an upper bound as

$$g(p, e) \lesssim g(p, 1) = \frac{p^2}{6} J_p^2(p) \sim \frac{p^2}{6} \left[\frac{\Gamma(1/3)}{2^{2/3} 3^{1/6} \pi p^{1/3}} \right]^2 = \frac{[\Gamma(1/3)]^2}{2^{7/3} 3^{4/3} \pi^2} p^{4/3}, \quad (\text{A3})$$

where we use Eq. (A1) in Ref. [31] at the second equality and we use the asymptotic formula for Bessel function at the third equality. Using this relation, Eq. (A2) becomes

$$\mathcal{F}(p) = p^{-13/3} \int_0^1 de f_{\nu,e,t}(\nu_p, e; t_0) g(p, e) \lesssim p^{-13/3} g(p, 1) \int_0^1 de f_{\nu,e,t}(\nu_p, e; t_0). \quad (\text{A4})$$

Next, we integrate

$$\int_0^1 de f_{\nu,e,t}(\nu_p, e; t_0) = \frac{2a_p}{3\nu_p} \int_0^1 de f(a_p, e; t_0), \quad (\text{A5})$$

in Eq. (A4) where the orbital frequency $\nu_p = \nu_{gw}/p$ is given in Eq. (4.1) and the semimajor axis a_p is given in Eq. (3.9).⁶ The distribution function at the present epoch, $f(a, e; t_0)$, is

⁵We have not proved this fact. However we confirmed this numerically.

⁶We add the subscript p to a in order to emphasize that the semimajor axis a depends on p for a fixed gravitational wave frequency ν_{gw} .

given by Eq. (3.8) and the initial distribution function, $f_i(a_i, e_i)$, is given by Eq. (2.8). The ranges of a_i and e_i are $0 < a_i < \infty$ and $\sqrt{1 - \beta^2} < e_i < 0$, respectively.

Since $g(p, e)$ has a peak at $e \sim 1$ for a large p , it is sufficient to consider only $1 - e^2 \ll 1$ case. When eccentricity is near 1, we can express a_i and e_i by a_p and e as

$$a_i = a_p u^{-2} [1 + u]^2, \quad (\text{A6})$$

$$1 - e_i^2 = (1 - e^2) u^2 [1 + u]^{-2}, \quad (\text{A7})$$

where

$$u = \left(\frac{a_p}{a_0} \right)^4 (1 - e^2)^{7/2}. \quad (\text{A8})$$

The above equations can be derived from Eqs. (3.3), (2.9) and the fact that the difference between the coalescence time at $t = t_f$ and that at $t = t_0$ is t_0 . For given a_p , there is e_p that satisfies $u = 1$ as

$$e_p = \sqrt{1 - \left(\frac{a_p}{a_0} \right)^{-8/7}}. \quad (\text{A9})$$

For $e_p < e < 1$, we can approximate Eqs. (A6) and (A7) as

$$\begin{aligned} a_i &\simeq a_p u^{-2}, \\ 1 - e_i^2 &\simeq (1 - e^2) u^2, \end{aligned} \quad (\text{A10})$$

since $u < 1$. For $0 < e < e_p$, we can approximate Eqs. (A6) and (A7) as

$$\begin{aligned} a_i &\simeq a_p, \\ 1 - e_i^2 &\simeq 1 - e^2, \end{aligned} \quad (\text{A11})$$

since $u > 1$. Note that Eq. (A11) is a good approximation for $u \gg 1$ even when $1 - e^2 \sim 1$.

We separate the integration range of Eq. (A5) into two parts, $0 < e < e_p$ and $e_p < e < 1$. In each range, we use the approximate relations of Eqs. (A10) and (A11). Firstly, we integrate Eq. (A5) in the range of $0 < e < e_p$. Since $e \simeq e_i$ for $0 < e < e_p$ and $\sqrt{1 - \beta^2} < e_i < 1$ have to be satisfied, the integration range is $\sqrt{1 - \beta^2} < e < e_p$. The present

distribution function $f(a_p, e; t_0)$ is the same as the initial distribution function $f_i(a_i, e_i)$, since the relations in Eq. (A11) are satisfied for $0 < e < e_p$. We perform the integration as

$$\begin{aligned}
\int_0^{e_p} de f_{\nu, e, t}(\nu_p, e; t_0) &= \frac{2a_p}{3\nu_p} \int_0^{e_p} de f(a_p, e; t_0) \\
&\simeq \frac{2a_p}{3\nu_p} \int_{\sqrt{1-\beta^2}}^{e_p} de f(a_p, e; t_0) \simeq \frac{2a_p}{3\nu_p} \int_{\sqrt{1-\beta^2}}^{e_p} de f_i(a_p, e) \\
&= \frac{1}{2\nu_p} \left(\frac{a_p}{\alpha\bar{x}} \right)^{3/4} \left\{ \exp \left[- \left(\frac{a_p}{\alpha\bar{x}} \right)^{3/4} \right] - \exp \left[- \frac{\beta}{(1-e_p^2)^{1/2}} \left(\frac{a_p}{\alpha\bar{x}} \right)^{3/4} \right] \right\} \\
&= \frac{1}{2\nu_p} \left(\frac{a_p}{\alpha\bar{x}} \right)^{3/4} \left\{ \exp \left[- \left(\frac{a_p}{\alpha\bar{x}} \right)^{3/4} \right] - \exp \left[- \beta \left(\frac{a_p}{a_0} \right)^{4/7} \left(\frac{a_p}{\alpha\bar{x}} \right)^{3/4} \right] \right\} \\
&\cong \begin{cases} 0 & a_p < \beta^{-4/7} a_0 \\ \frac{1}{2\nu_p} \beta \left(\frac{a_p}{\alpha\bar{x}} \right)^{3/2} \left(\frac{a_p}{a_0} \right)^{4/7} & \beta^{-4/7} a_0 < a_p \lesssim \beta^{-28/37} a_0^{16/37} (\alpha\bar{x})^{21/37} \\ \frac{1}{2\nu_p} \left(\frac{a_p}{\alpha\bar{x}} \right)^{3/4} & \beta^{-28/37} a_0^{16/37} (\alpha\bar{x})^{21/37} \lesssim a_p < \alpha\bar{x} \\ 0 & \alpha\bar{x} < a_p \\ 0 & p < p_1 \\ \frac{1}{2\nu_{gw}} \beta \left(\frac{a_{gw}}{\alpha\bar{x}} \right)^{3/2} \left(\frac{a_{gw}}{a_0} \right)^{4/7} p^{50/21} & p_1 < p \lesssim p_2 \\ \frac{1}{2\nu_{gw}} \left(\frac{a_{gw}}{\alpha\bar{x}} \right)^{3/4} p^{3/2} & p_2 \lesssim p < p_3 \\ 0 & p_3 < p, \end{cases} \quad (A12) \\
\end{aligned}$$

where a_{gw} is defined as

$$a_{gw} = (2\pi\nu_{gw})^{-2/3} [G(M_{BH1} + M_{BH2})]^{1/3} = p^{-2/3} a_p, \quad (A13)$$

and

$$p_1 = \beta^{-6/7} \left(\frac{a_{gw}}{a_0} \right)^{-3/2} \quad (A14)$$

$$p_2 = \beta^{-42/37} \left(\frac{a_{gw}}{a_0} \right)^{-24/37} \left(\frac{a_{gw}}{\alpha\bar{x}} \right)^{-63/74} \quad (A15)$$

$$p_3 = \left(\frac{a_{gw}}{\alpha\bar{x}} \right)^{-3/2}. \quad (A16)$$

In Eq. (A12), the first range of p is determined by the condition, $e_p < \sqrt{1-\beta^2}$, where the integration range becomes zero. The second range of p is determined by the condition, $\beta(a_p/a_0)^{4/7}(a_p/\alpha\bar{x})^{3/4} < 1$, where we can expand out the second exponential in Eq. (A12)

with good accuracy. The third range of p is determined by the condition, $(a_p/\alpha\bar{x})^{3/4} = 1$, where the integration begins to damp exponentially.

Secondly, we integrate Eq. (A5) in the range of $e_p < e < 1$. Using the relations in Eq. (A10), we perform the integration as

$$\begin{aligned}
\int_{e_p}^1 de f_{\nu,e,t}(\nu_p, e; t_0) &= \frac{2a_p}{3\nu_p} \int_{e_p}^1 de f(a_p, e; t_0) \simeq \frac{2a_p}{3\nu_p} \int_{e_p}^1 de \frac{a_i}{a_p} \left(\frac{1 - e_i^2}{1 - e^2} \right)^{3/2} f_i(a_i, e_i) \\
&= \int_{e_p}^1 e_i de \frac{1}{2\nu_p} \frac{\beta}{(1 - e_i^2)^{3/2}} \frac{a_p a_i^{1/2}}{(\alpha\bar{x})^{3/2}} \frac{a_i}{a_p} \left(\frac{1 - e_i^2}{1 - e^2} \right)^{3/2} \\
&\quad \times \exp \left[-\frac{\beta}{(1 - e_i^2)^{1/2}} \left(\frac{a_i}{\alpha\bar{x}} \right)^{3/4} \right] \\
&\simeq \int_{e_p}^1 ede \frac{1}{2\nu_p} \frac{\beta}{(1 - e^2)^{3/2}} \left(\frac{a_p}{\alpha\bar{x}} \right)^{3/2} u^{-3} \exp \left[-\frac{\beta}{(1 - e^2)^{1/2}} \left(\frac{a_p}{\alpha\bar{x}} \right)^{3/4} u^{-5/2} \right] \\
&= \int_{e_p}^1 ede \frac{1}{2\nu_p} \beta \left(\frac{a_p}{\alpha\bar{x}} \right)^{3/2} \left(\frac{a_p}{a_0} \right)^{-12} (1 - e^2)^{-12} \\
&\quad \times \exp \left[-\beta \left(\frac{a_p}{\alpha\bar{x}} \right)^{3/4} \left(\frac{a_p}{a_0} \right)^{-10} (1 - e^2)^{-37/4} \right] \\
&= \frac{1}{37\nu_p} \beta^{-7/37} \left(\frac{a_p}{\alpha\bar{x}} \right)^{45/74} \left(\frac{a_p}{a_0} \right)^{-4/37} \\
&\quad \times \int_{\beta(a_p/\alpha\bar{x})^{3/4}(a_p/a_0)^{-10}(1-e_p^2)^{-37/4}}^{\infty} d\xi \xi^{7/37} \exp(-\xi) \\
&\lesssim \frac{1}{37\nu_{gw}} \beta^{-7/37} \left(\frac{a_{gw}}{\alpha\bar{x}} \right)^{45/74} \left(\frac{a_{gw}}{a_0} \right)^{-4/37} \Gamma \left(\frac{44}{37} \right) p^{4/3}.
\end{aligned} \tag{A17}$$

Using Eqs. (A3), (A12) and (A17), $\mathcal{F}(p)$ in Eq. (A4) can be approximated as

$$\begin{aligned}
\mathcal{F}(p) &\lesssim p^{-13/3} g(p, 1) \int de f_{\nu,e,t}(\nu_p, e; t_0) \\
&\sim \frac{[\Gamma(1/3)]^2}{2^{7/3} 3^{4/3} \pi^2} p^{-3} \left[\int_{e_p}^1 de f_{\nu,e,t}(\nu_p, e; t_0) + \int_0^{e_p} de f_{\nu,e,t}(\nu_p, e; t_0) \right] \\
&\simeq \begin{cases} \frac{[\Gamma(1/3)]^2}{2^{7/3} 3^{4/3} \pi^2} p^{-3} \left[\frac{\beta^{-7/37}}{37\nu_{gw}} \left(\frac{a_{gw}}{\alpha\bar{x}} \right)^{45/74} \left(\frac{a_{gw}}{a_0} \right)^{-4/37} \Gamma \left(\frac{44}{37} \right) p^{4/3} + 0 \right] & : p < p_1 \\ \frac{[\Gamma(1/3)]^2}{2^{7/3} 3^{4/3} \pi^2} p^{-3} \left[\frac{\beta^{-7/37}}{37\nu_{gw}} \left(\frac{a_{gw}}{\alpha\bar{x}} \right)^{45/74} \left(\frac{a_{gw}}{a_0} \right)^{-4/37} \Gamma \left(\frac{44}{37} \right) p^{4/3} + \frac{\beta}{2\nu_{gw}} \left(\frac{a_{gw}}{\alpha\bar{x}} \right)^{3/2} \left(\frac{a_{gw}}{a_0} \right)^{4/7} p^{50/21} \right] & : p_1 < p \lesssim p_2 \\ \frac{[\Gamma(1/3)]^2}{2^{7/3} 3^{4/3} \pi^2} p^{-3} \left[\frac{\beta^{-7/37}}{37\nu_{gw}} \left(\frac{a_{gw}}{\alpha\bar{x}} \right)^{45/74} \left(\frac{a_{gw}}{a_0} \right)^{-4/37} \Gamma \left(\frac{44}{37} \right) p^{4/3} + \frac{1}{2\nu_{gw}} \left(\frac{a_{gw}}{\alpha\bar{x}} \right)^{3/4} p^{3/2} \right] & : p_2 \lesssim p < p_3 \\ \frac{[\Gamma(1/3)]^2}{2^{7/3} 3^{4/3} \pi^2} p^{-3} \left[\frac{\beta^{-7/37}}{37\nu_{gw}} \left(\frac{a_{gw}}{\alpha\bar{x}} \right)^{45/74} \left(\frac{a_{gw}}{a_0} \right)^{-4/37} \Gamma \left(\frac{44}{37} \right) p^{4/3} + 0 \right] & : p_3 < p. \end{cases} \tag{A18}
\end{aligned}$$

The summation of $\mathcal{F}(p)$ with respect to p in Eq. (A1) can be approximated as the integration with respect to p . The integration of $\mathcal{F}(p)$ can be performed as

$$\begin{aligned}
\mathcal{S}(p_0) &:= \sum_{p=p_0}^{\infty} \mathcal{F}(p) \sim \int_{p_0}^{\infty} dp \mathcal{F}(p) = \int_{p_0}^{p_2} dp \mathcal{F}(p) + \int_{p_2}^{p_3} dp \mathcal{F}(p) + \int_{p_3}^{\infty} dp \mathcal{F}(p) \\
&\lesssim \frac{[\Gamma(1/3)]^2}{2^{7/3} 3^{4/3} \pi^2} \left\{ \frac{\beta^{-7/37}}{37 \nu_{gw}} \left(\frac{a}{\alpha \bar{x}} \right)^{45/74} \left(\frac{a}{a_0} \right)^{-4/37} \Gamma \left(\frac{44}{37} \right) \left[-\frac{3}{2} p^{-2/3} \right] \Big|_{p=p_0}^{p=\infty} \right. \\
&\quad + \frac{\beta}{2\nu_{gw}} \left(\frac{a}{\alpha \bar{x}} \right)^{3/2} \left(\frac{a}{a_0} \right)^{4/7} \left[\frac{21}{8} p^{8/21} \right] \Big|_{p=p_0}^{p=p_2} + \frac{1}{2\nu_{gw}} \left(\frac{a}{\alpha \bar{x}} \right)^{3/4} \left[-2p^{-1/2} \right] \Big|_{p=p_2}^{p=p_3} \Big\} \\
&= \frac{[\Gamma(1/3)]^2}{2^{7/3} 3^{4/3} \pi^2 \nu_{gw}} \left\{ \frac{3}{74} \beta^{-7/37} \left(\frac{a}{\alpha \bar{x}} \right)^{45/74} \left(\frac{a}{a_0} \right)^{-4/37} \Gamma \left(\frac{44}{37} \right) p_0^{-2/3} \right. \\
&\quad + \frac{37}{16} \beta^{21/37} \left(\frac{a}{\alpha \bar{x}} \right)^{87/74} \left(\frac{a}{a_0} \right)^{12/37} - \left(\frac{a}{\alpha \bar{x}} \right)^{3/2} - \frac{21}{16} \beta \left(\frac{a}{\alpha \bar{x}} \right)^{3/2} \left(\frac{a}{a_0} \right)^{4/7} p_0^{8/21} \Big\}, \quad (\text{A19})
\end{aligned}$$

where we consider the case of $p_1 < p_0 < p_2$. All the contribution from high p -th harmonics with $p_0 \leq p$ to the gravitational wave flux in Eq.(A1) is given by

$$F_{\nu}^{(p \geq p_0)}(\nu_{gw}) \lesssim IL_c \nu_{gw}^{10/3} \mathcal{S}(p_0). \quad (\text{A20})$$

In Fig. 13, we plot $F_{\nu}^{(p \geq p_0)}(\nu_{gw})/F_{\nu}^{(p \leq p_0)}(\nu_{gw})$ for $M_{BH} = 0.5M_{\odot}$, $\Omega h^2 = 0.1$ and $p_0 = 1000$, where $F_{\nu}^{(p \leq p_0)}(\nu_{gw})$ is the gravitational wave flux summed up till $p = p_0$. The error of $F_{\nu}^{(p \leq p_0)}(\nu_{gw})$ is less than a few percent at $\nu_{gw} \lesssim 10^{-2.5}$ Hz. At $\nu_{gw} \gtrsim 10^{-2.5}$ Hz, the error of $F_{\nu}^{(p \leq p_0)}(\nu_{gw})$ seems to be large, however this is merely overestimation of the error. As we can see in Fig. 3, the results summed up till $p = 10$ coincide with the results summed up till $p = 1000$ very well at $\nu_{gw} \gtrsim 10^{-2.5}$ Hz, and this indicates that the error due to the cutoff of high harmonics is small at $\nu_{gw} \gtrsim 10^{-2.5}$ Hz. To conclude, it is sufficient to sum up till $p \sim 1000$ in Eq. (A1) for a few percent precision.

REFERENCES

- [1] C. Alcock *et al.*, *Astrophys. J.* **486**, 697 (1997).
- [2] K. Cook, in *Proceedings of the 4th International workshop on gravitational microlensing surveys*, 1998.
- [3] J. N. Bahcall, C. Flynn, A. Gould, and S. Kirhakos, *Astrophys. J. Lett.* **435**, L51 (1994).
- [4] C. Flynn, A. Gould, and J. N. Bahcall, *Astrophys. J. Lett.* **466**, L55 (1996).
- [5] D. S. Graff and K. Freese, *Astrophys. J. Lett.* **456**, L49 (1996); **467**, L65 (1996).
- [6] D. Ryu, K. A. Olive, and J. Silk, *Astrophys. J.* **353**, 81 (1990).
- [7] G. Chabrier, L. Segretain, and D. Mera, *Astrophys. J. Lett.* **468**, L21 (1996).
- [8] F. C. Adams and G. Laughlin, *Astrophys. J.* **468**, 586 (1996).
- [9] B. D. Fields, G. J. Mathews, and D. N. Schramm, *Astrophys. J.* **483**, 625 (1997).
- [10] S. Charlot and J. Silk, *Astrophys. J.* **445**, 124 (1995).
- [11] B. K. Gibson and J. R. Mould, *Astrophys. J.* **482**, 98 (1997).
- [12] R. Canal, J. Isern, and P. Ruiz-Lapuente, *Astrophys. J. Lett.* **488**, L35 (1997).
- [13] M. Honma and Y. Kan-ya, *Astrophys. J. Lett.* **503**, L139 (1998).
- [14] J. Binney, [astro-ph/9809097](#).
- [15] B. M. S. Hansen, *Nature* **394**, 860 (1998).
- [16] C. Alcock *et al.*, *Astrophys. J. Lett.* **491**, L11 (1997).
- [17] N. Palanque-Delabrouille *et al.*, *Astron. Astrophys.* **332**, 1 (1998).
- [18] T. Nakamura, Y. Kan-ya, and R. Nishi, *Astrophys. J. Lett.* **473**, L99 (1996).
- [19] K. C. Sahu, *Nature* **370**, 275 (1994).

[20] H. S. Zhao, astro-ph/9606166; Mon. Not. R. Astron. Soc. **294**, 139 (1998).

[21] N. W. Evans, G. Gyuk, M. S. Turner and J. Binney, *Astrophys. J. Lett.* **501**, L45 (1998).

[22] E. I. Gates, G. Gyuk, G. P. Holder and M. S. Turner, *Astrophys. J. Lett.* **500**, L145 (1998).

[23] J. Yokoyama, *Astron. Astrophys.* **318**, 673 (1997).

[24] M. Kawasaki, N. Sugiyama, and T. Yanagida, *Phys. Rev. D* **57**, 6050 (1998).

[25] K. Jedamzik, *Phys. Rev. D* **55**, 5871 (1997).

[26] Y. Fujita, S. Inoue, T. Nakamura, T. Manmoto, and K. E. Nakamura, *Astrophys. J. Lett.* **495**, L85 (1998).

[27] T. Nakamura, M. Sasaki, T. Tanaka, and K. S. Thorne, *Astrophys. J. Lett.* **487**, L139 (1997).

[28] K. Ioka, T. Chiba, T. Tanaka, and T. Nakamura, *Phys. Rev. D* **58**, 063003 (1998).

[29] B. J. Carr and S. W. Hawking, *Mon. Not. R. Astron. Soc.* **168**, 399 (1974); B. J. Carr, *Astrophys. J.* **201**, 1 (1975); J. C. Niemeyer and K. Jedamzik, *Phys. Rev. Lett.* **80**, 5481 (1998).

[30] P. C. Peters, *Phys. Rev. B* **136**, 1224 (1964).

[31] P. C. Peters and J. Mathews, *Phys. Rev.* **131**, 435 (1963).

[32] D. Hils, *Astrophys. J.* **381**, 484 (1991).

[33] T. Nakamura, Y. Kan-ya, and R. Nishi, *Astrophys. J.* **473**, L99 (1996).

[34] K. S. Thorne, in *300 Years of Gravitation*, edited by S. W. Hawking and W. Israel (Cambridge University Press, Cambridge, England, 1987), pp. 330-458.

- [35] T. P. Walker *et al.*, *Astrophys. J.* **376**, 51 (1991).
- [36] V. M. Kaspi, J. H. Taylor, and M. F. Ryba, *Astrophys. J.* **428**, 713 (1994).
- [37] S. E. Thorsett and R. J. Dewey, *Phys. Rev. D* **53**, 3468 (1996).
- [38] C. R. Gwinn *et al.*, *Astrophys. J.* **485**, 87 (1997).
- [39] D. Hils, P. L. Bender, and R. F. Webbink, *Astrophys. J.* **360**, 75 (1990).
- [40] D. I. Kosenko and K. A. Postnov, *Astron. Astrophys.* **336**, 786 (1998).
- [41] K. A. Postnov and M. E. Prokhorov, *Astrophys. J.* **494**, 674 (1998); *Astrophys. J.* **502**, 498 (1998); *Astron. Astrophys.* **327**, 428 (1997).
- [42] R. F. Webbink, *Astrophys. J.* **277**, 355 (1984).
- [43] K. Danzmann *et al.*, LISA Pre-Phase A Report, Max-Plank-Institut fur Guantenoptik, Report No. MPQ 208, Garching, Germany, 1996.
- [44] P. L. Bender and D. Hils, *Class. Quantum. Grav.* **14**, 1439 (1997).
- [45] B. F. Schutz, gr-qc/9710080.
- [46] C. Cutler, *Phys. Rev. D* **57**, 7089 (1998).
- [47] M. Shibata, *Phys. Rev. D* **50**, 6297 (1994).
- [48] D. Hils and P. L. Bender, *Astrophys. J. Lett.* **445**, L7 (1995).
- [49] S. Sigurdsson, *Class. Quantum. Grav.* **14**, 1425 (1997).
- [50] G. D. Quinlan and S. L. Shapiro, *Astrophys. J.* **343**, 725 (1989); **356**, 483 (1990).
- [51] D. P. Bennett *et al.*, *Nucl. Phys. B (Proc. Suppl.)* **51B**, 152 (1996).
- [52] C. Afonso *et al.*, *Astron. Astrophys.* **337**, L17 (1998).
- [53] M. D. Albrow *et al.*, astro-ph/9807086.

[54] C. Alcock *et al*, astro-ph/9807163.

FIGURE CAPTION

Fig.1. The probability distribution function $f_{\nu,e,t}(\nu_p, e; t_1)$ as a function of eccentricity e for (a) $\nu_p = 10^{-1}$ Hz, (b) $\nu_p = 10^{-2}$ Hz, (c) $\nu_p = 10^{-3}$ Hz and (d) $\nu_p = 10^{-4}$ Hz, at present epoch, i.e. we set $t_1 = t_0 = 10^{10}$ yr. Here we adopt $M_{BH} = 0.5M_\odot$ and $\Omega h^2 = 0.1$.

Fig.2. The shape factor \tilde{I} defined in Eq. (4.13) as a function of the core radius D_a for three values of λ .

Fig.3. The solid line is the spectral density of the gravitational wave strain amplitude $h_\nu^{halo}/\sqrt{\tilde{I}}$ for the halo background gravitational waves for $M_{BH} = 0.5M_\odot$ and $\Omega h^2 = 0.1$. The long dashed line is the spectral density obtained by the summation up to $p = 10$ in Eq. (4.14). The dotted line is the approximate spectral density, replacing the flux F_ν in Eq. (4.15) with the approximate flux F_ν in Eq. (4.16). The approximation is valid for $e \ll 1$. Note that $h_\nu^{halo}/\sqrt{\tilde{I}}$ does not depend on the halo shape factor, \tilde{I} .

Fig.4. The solid line is $d\Omega_{GW}/d(\ln R)$ in Eq. (5.8) as a function of R/R_0 for $M_{BH} = 0.5M_\odot$ and $\Omega_{BH}h^2 = 0.1$ at four frequencies. The dotted line is the approximation of $d\Omega_{GW}/d(\ln R)$, replacing the luminosity \mathcal{L}_{GW} in Eq. (5.7) with the approximate luminosity \mathcal{L}_{GW} in Eq. (5.10). The approximation is valid for $e \ll 1$. Solid and dotted lines are almost same for high frequencies.

Fig.5. The energy density of the cosmological gravitational wave background per logarithmic frequency $\Omega_{GW}(\nu_{gw})$ as a function of the gravitational wave frequency ν_{gw} , where we summed up to $p = 10$ in Eq. (5.7). We adopt $M_{BH} = 0.5M_\odot$ and $\Omega h^2 = 0.1$.

Fig.6. The spectral density h_ν for the cosmological gravitational wave background in Eq. (5.9) by the solid line, for the halo background in Eq. (4.15) by the dashed line, the CWDBs background by the cross, and the instrumental noise in Eqs. (6.1) and (6.2) by the dotted line. We adopt $M_{BH} = 0.5M_\odot$ and $\Omega h^2 = 0.1$. The shape factor \tilde{I} in Eq. (4.13) for the halo background is taken to be 7.

Fig.7. The shape factor K defined in Eq. (7.10) as a function of the core radius D_a for three values of λ .

Fig.8. The expected number of the individual sources per logarithmic frequency in each harmonic $N^{(p)}(\nu_{gw})$ in Eq. (7.5) for $p = 1, 2, 3, 4, 5$, We adopt $\lambda = 1$, $D_a = 5$ kpc, $M_{BH} = 0.5M_{\odot}$ and $\Omega h^2 = 0.1$.

Fig.9. The maximum distance $D_{max}^{(p)}(\nu_{gw}, e_{peak})$ to a source whose gravitational wave amplitude exceeds the threshold value for $p = 1, 2, 3, 4, 5$, where e_{peak} is the eccentricity at which the distribution function $f_{\nu,e,t}(\nu_p, e; t_0)$ is maximum. The background is due to cosmological BHMACHO binaries and instruments. We adopt $M_{BH} = 0.5M_{\odot}$, $\Omega h^2 = 0.1$, $\lambda = 1$ and $D_a = 5$ kpc.

Fig.10. The total expected number of the individual sources per logarithmic frequency $N(\nu_{gw})$ in Eq. (7.7). The background is due to cosmological BHMACHO binaries and instruments. The dotted line is the expected number using Eq. (7.9) with $K=0.8$, which is valid for $D_{max}^{(p)}(\nu_{gw}, e) \ll D_0$. The dashed line is the expected number using Eq. (7.16), which is valid for $D_{max}^{(p)}(\nu_{gw}, e) \gg D_0$. We adopt $M_{BH} = 0.5M_{\odot}$, $\Omega h^2 = 0.1$, $\lambda = 1$ and $D_a = 5$ kpc.

Fig.11. The maximum distance $D_{max}^{(p)}(\nu_{gw}, e_{peak})$ to a source whose gravitational wave amplitude exceeds the threshold value for $p = 1, 2, 3, 4, 5$, where e_{peak} is the eccentricity at which the distribution function $f_{\nu,e,t}(\nu_p, e; t_0)$ is maximum. The background is due to CWDBs and instruments. We adopt $M_{BH} = 0.5M_{\odot}$, $\Omega h^2 = 0.1$, $\lambda = 1$ and $D_a = 5$ kpc.

Fig.12. The total expected number of the individual sources per logarithmic frequency $N(\nu_{gw})$ in Eq. (7.7). Solid line is the case that the background is due to CWDBs and instruments, and dotted line is the case that the background is due to cosmological BHMACHO binaries and instruments. We adopt $M_{BH} = 0.5M_{\odot}$, $\Omega h^2 = 0.1$, $\lambda = 1$ and $D_a = 5$ kpc.

Fig.13. $F_\nu^{(p \geq p_0)}(\nu_{gw})/F_\nu^{(p \leq p_0)}(\nu_{gw})$ for $M_{BH} = 0.5M_\odot$, $\Omega h^2 = 0.1$ and $p_0 = 1000$, where $F_\nu^{(p \leq p_0)}(\nu_{gw})$ is the gravitational wave flux summed up till $p = p_0$ in Eq. (4.14) or Eq. (A1). The dotted line is the three percent error line, i.e., $F_\nu^{(p \geq p_0)}(\nu_{gw})/F_\nu^{(p \leq p_0)}(\nu_{gw}) = 0.03$.

TABLES

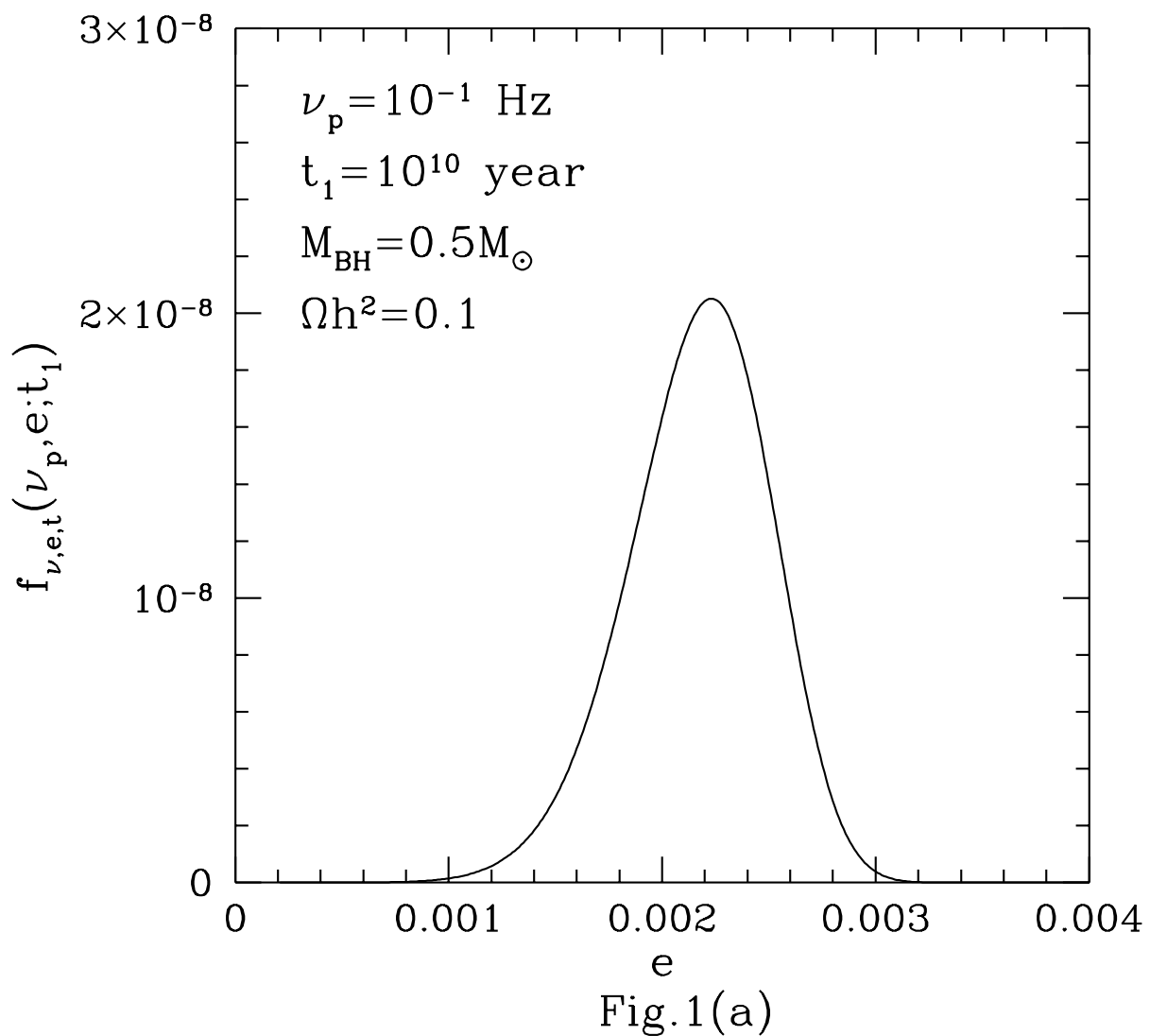
TABLE I. The spectral density of the gravitational wave strain amplitude $h_\nu^{halo}/\tilde{I}^{1/2}$ [Hz $^{-1/2}$] for the halo gravitational wave background in Eq. (4.15). The shape factor \tilde{I} is shown in Fig. 2

$\log(\nu_{gw}[\text{Hz}])$	$\log(h_\nu^{halo}/\tilde{I}^{1/2}[\text{Hz}^{-1/2}])$					
	$M_{BH} = 0.5M_\odot$		$M_{BH} = 0.05M_\odot$		$M_{BH} = 5M_\odot$	
	$\Omega h^2 = 0.1$	$\Omega h^2 = 0.5$	$\Omega h^2 = 0.1$	$\Omega h^2 = 0.5$	$\Omega h^2 = 0.1$	$\Omega h^2 = 0.5$
-1.00	-21.18	-21.03	-21.58	-21.43	-20.78	-20.63
-1.20	-20.95	-20.80	-21.35	-21.20	-20.55	-20.40
-1.40	-20.72	-20.56	-21.11	-20.96	-20.31	-20.16
-1.60	-20.48	-20.33	-20.86	-20.72	-20.08	-19.93
-1.80	-20.25	-20.10	-20.58	-20.46	-19.85	-19.70
-2.00	-20.01	-19.86	-20.32	-20.18	-19.61	-19.46
-2.20	-19.77	-19.62	-20.14	-19.94	-19.38	-19.23
-2.40	-19.50	-19.37	-20.08	-19.82	-19.15	-19.00
-2.60	-19.22	-19.09	-20.10	-19.79	-18.91	-18.76
-2.80	-19.01	-18.83	-20.17	-19.83	-18.67	-18.52
-3.00	-18.90	-18.66	-20.23	-19.90	-18.42	-18.28
-3.20	-18.89	-18.60	-20.25	-19.95	-18.14	-18.01
-3.40	-18.95	-18.62	-20.23	-19.95	-17.89	-17.73
-3.60	-19.02	-18.68	-20.20	-19.93	-17.74	-17.52
-3.80	-19.06	-18.74	-20.17	-19.90	-17.70	-17.42
-4.00	-19.05	-18.76	-20.15	-19.87	-17.73	-17.41
-4.20	-19.02	-18.74	-20.14	-19.85	-17.80	-17.46
-4.40	-18.99	-18.71	-20.13	-19.84	-17.85	-17.53

TABLE II. The spectral density of the gravitational wave strain amplitude h_ν^{cos} [Hz $^{-1/2}$] for the cosmological gravitational wave background in Eq. (5.9).

$\log(\nu_{gw}[\text{Hz}])$	$\log(h_\nu^{cos}[\text{Hz}^{-1/2}])$					
	$M_{BH} = 0.5M_\odot$		$M_{BH} = 0.05M_\odot$		$M_{BH} = 5M_\odot$	
	$\Omega h^2 = 0.1$	$\Omega h^2 = 0.5$	$\Omega h^2 = 0.1$	$\Omega h^2 = 0.5$	$\Omega h^2 = 0.1$	$\Omega h^2 = 0.5$
-1.00	-20.48	-19.96	-20.88	-20.36	-20.08	-19.56
-1.20	-20.24	-19.73	-20.64	-20.13	-19.84	-19.32
-1.40	-20.01	-19.49	-20.41	-19.89	-19.61	-19.09
-1.60	-19.78	-19.26	-20.17	-19.66	-19.38	-18.86
-1.80	-19.54	-19.03	-19.93	-19.41	-19.14	-18.62
-2.00	-19.31	-18.79	-19.68	-19.16	-18.91	-18.39
-2.20	-19.07	-18.56	-19.45	-18.93	-18.68	-18.16
-2.40	-18.83	-18.32	-19.25	-18.72	-18.44	-17.92
-2.60	-18.59	-18.07	-19.08	-18.56	-18.21	-17.69
-2.80	-18.34	-17.82	-18.93	-18.42	-17.97	-17.46
-3.00	-18.13	-17.60	-18.79	-18.30	-17.73	-17.22
-3.20	-17.95	-17.43	-18.67	-18.18	-17.49	-16.98
-3.40	-17.79	-17.28	-18.58	-18.07	-17.24	-16.73
-3.60	-17.65	-17.15	-18.54	-17.98	-17.02	-16.49
-3.80	-17.53	-17.03	-18.55	-17.92	-16.83	-16.30
-4.00	-17.42	-16.92	-18.58	-17.92	-16.66	-16.14
-4.20	-17.36	-16.82	-18.61	-17.95	-16.51	-16.01
-4.40	-17.35	-16.75	-18.60	-17.98	-16.38	-15.89

FIGURES



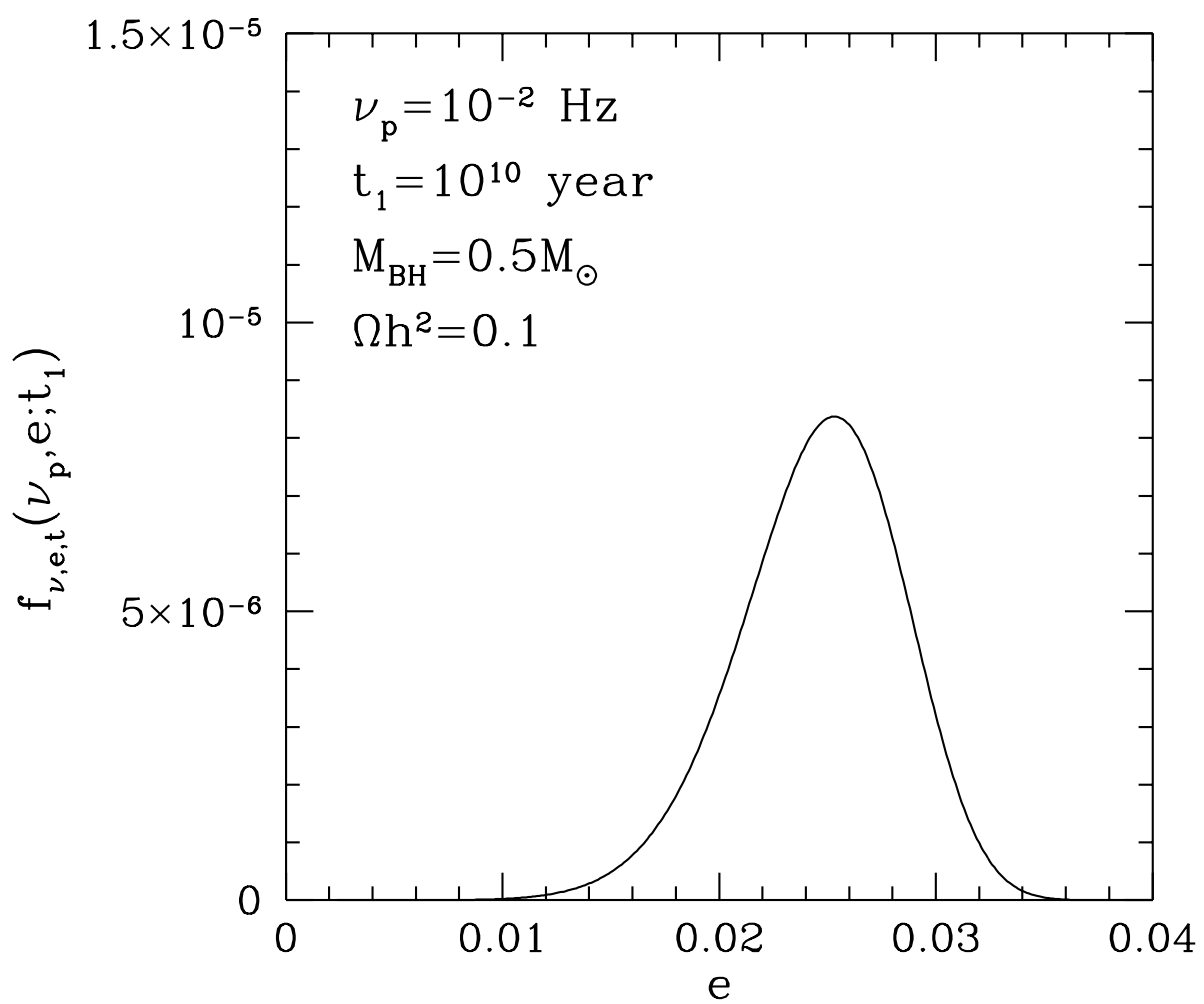
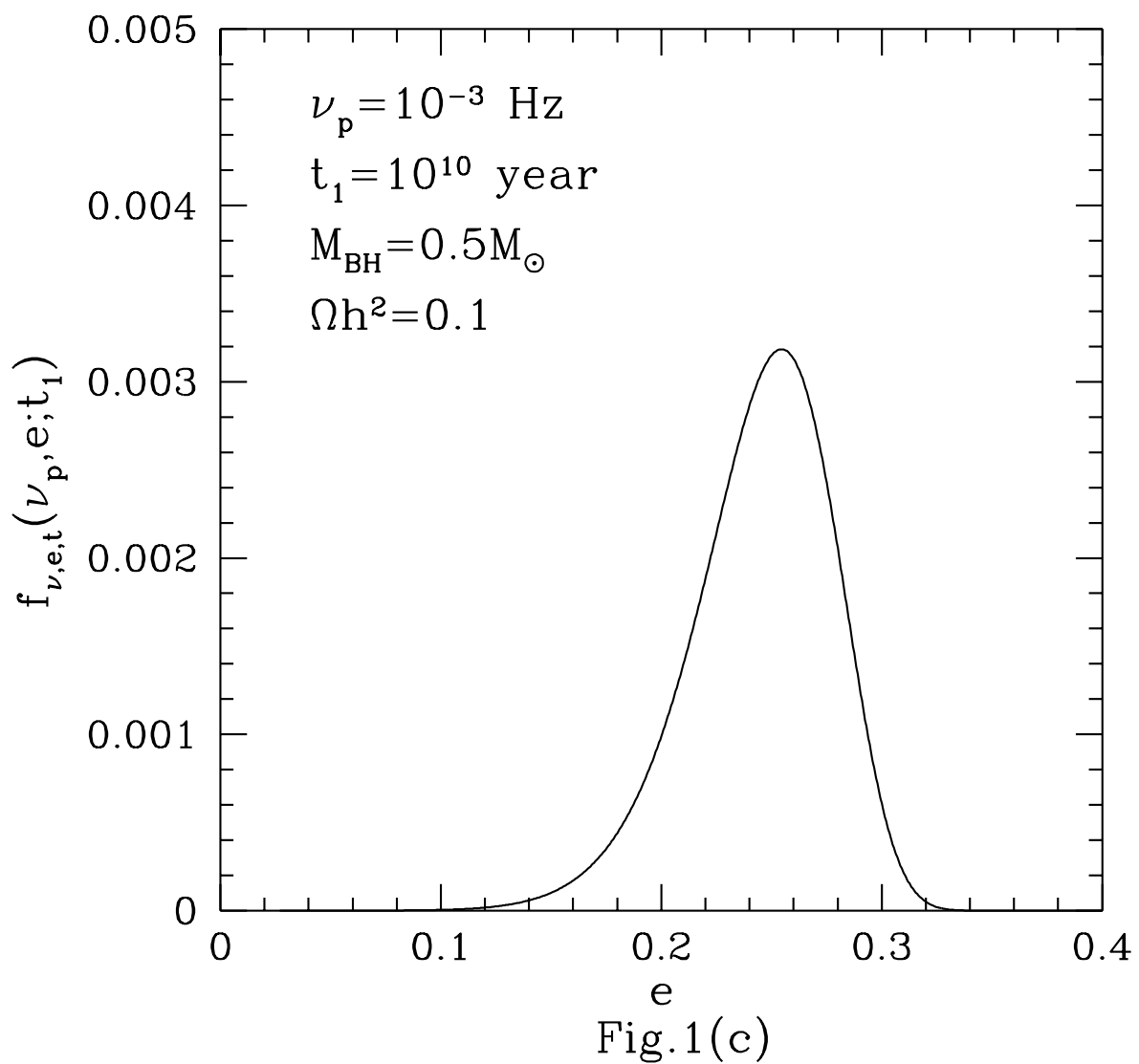
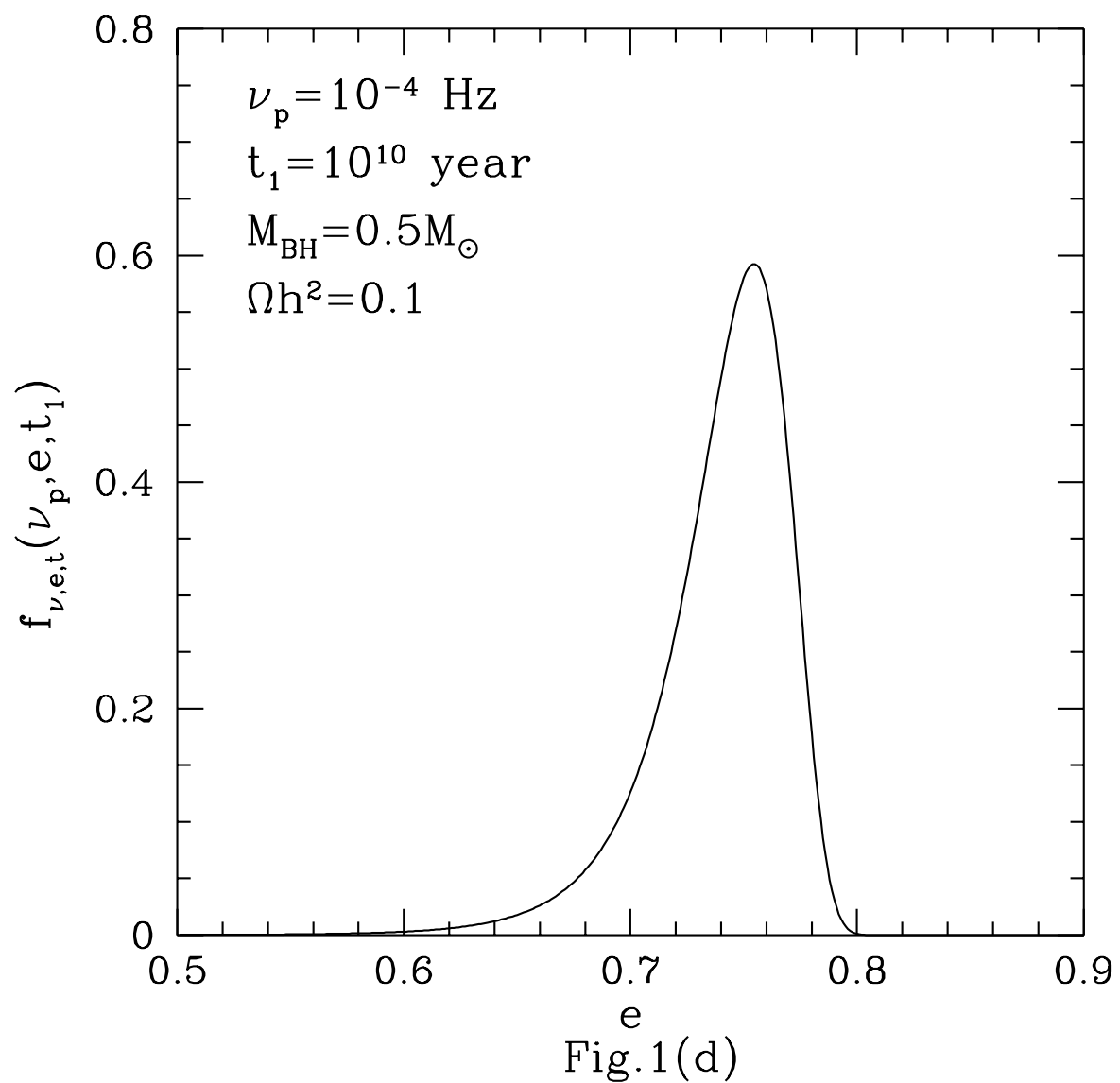
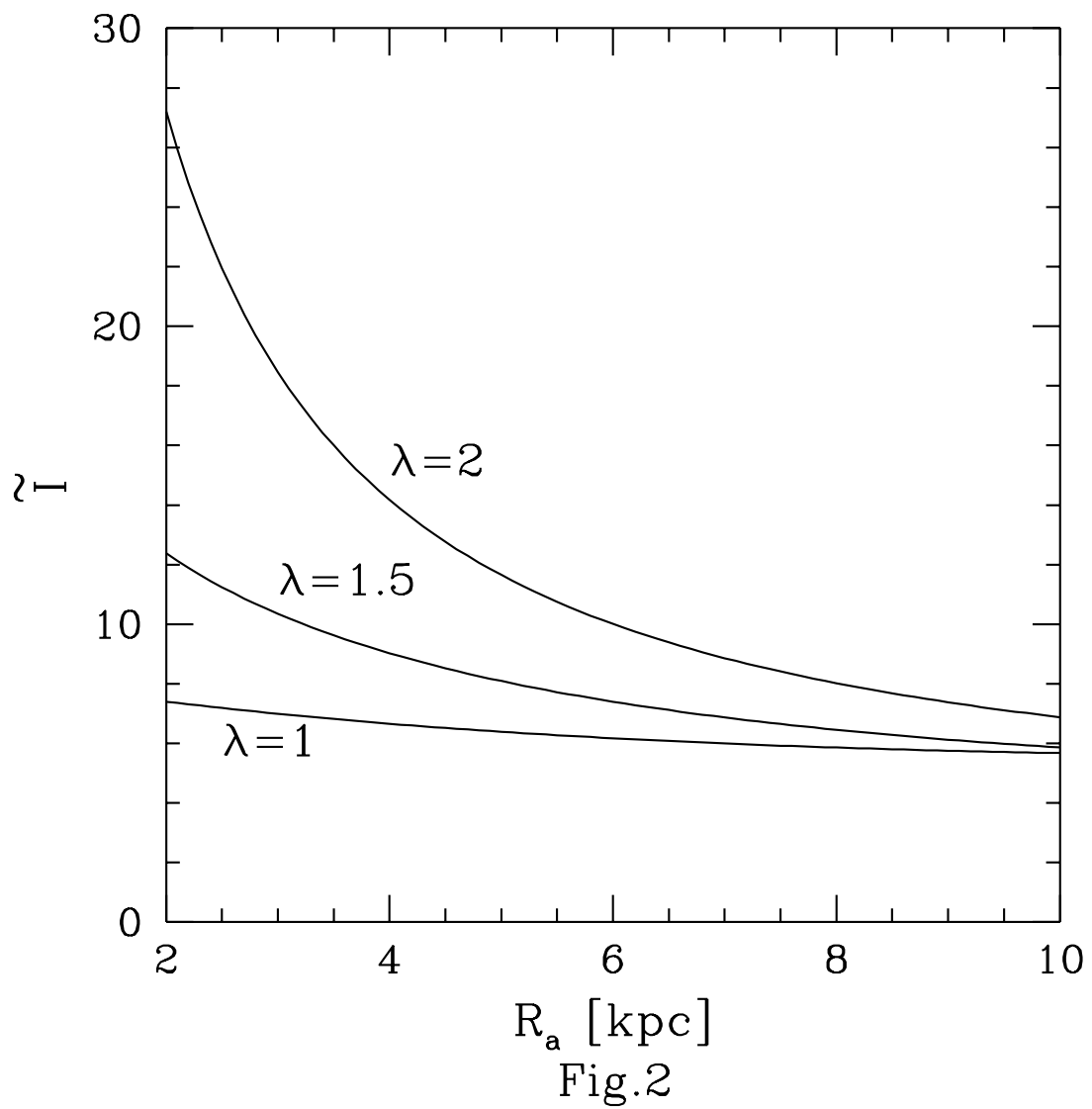


Fig.1(b)







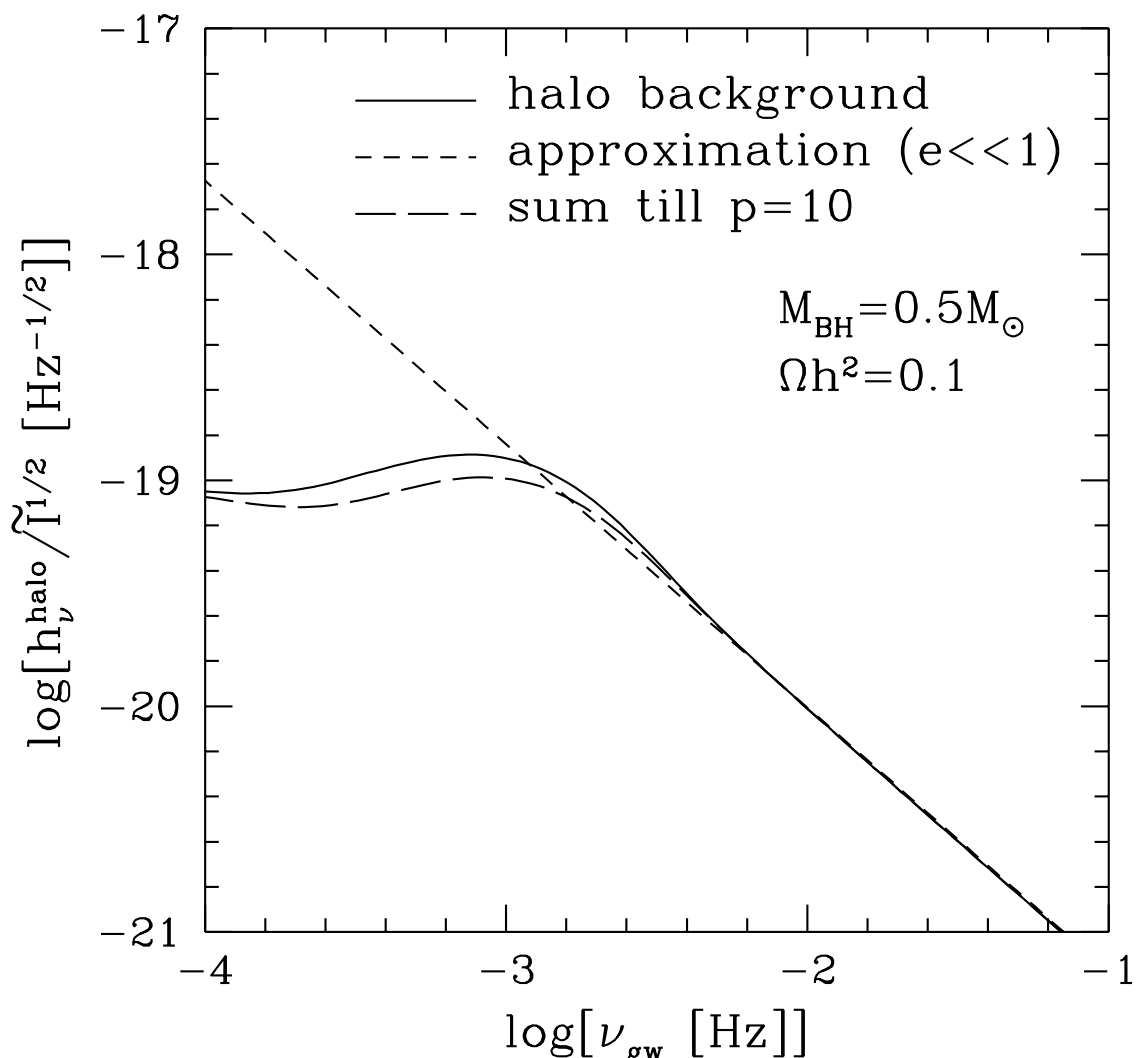


Fig.3

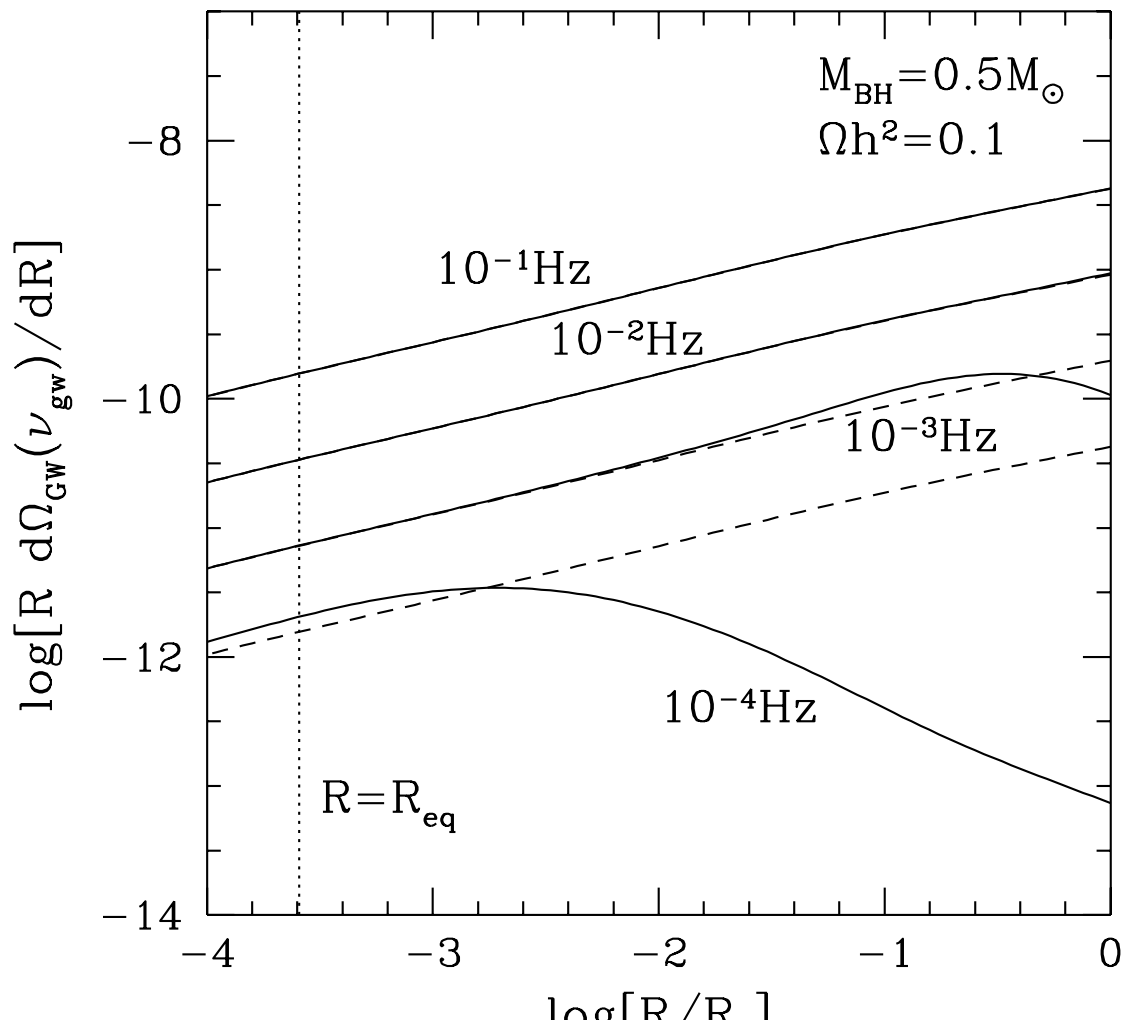


Fig.4

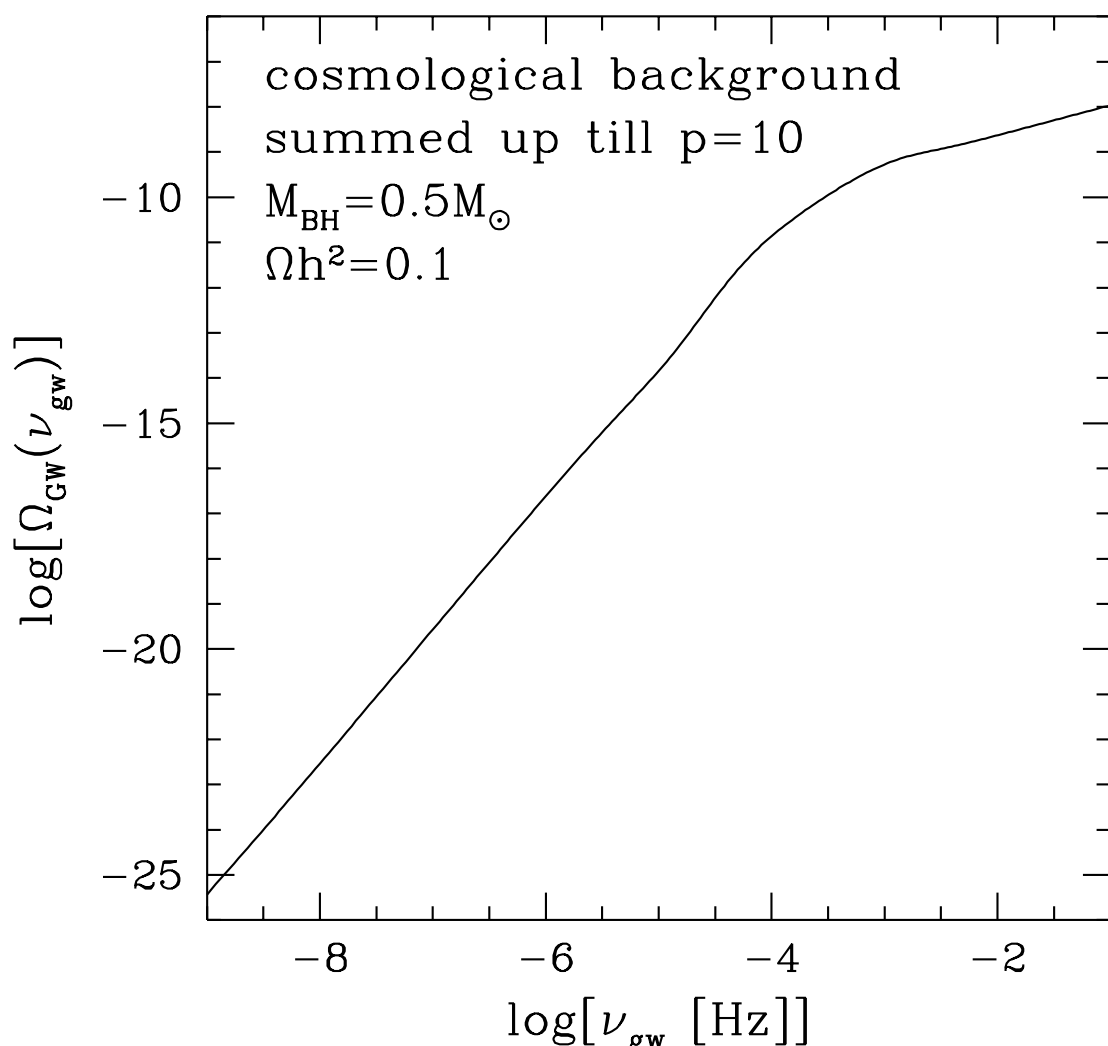


Fig.5

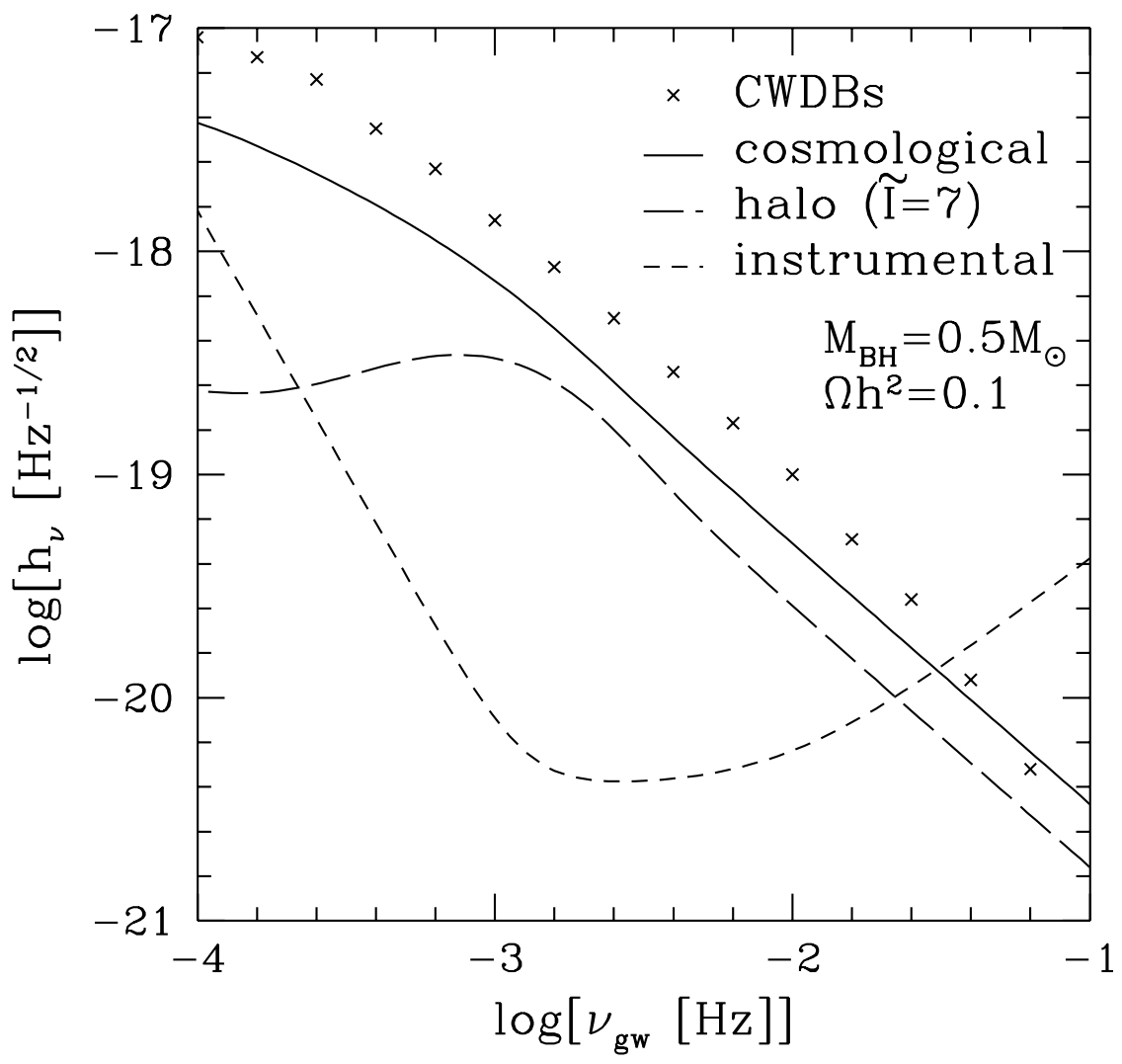
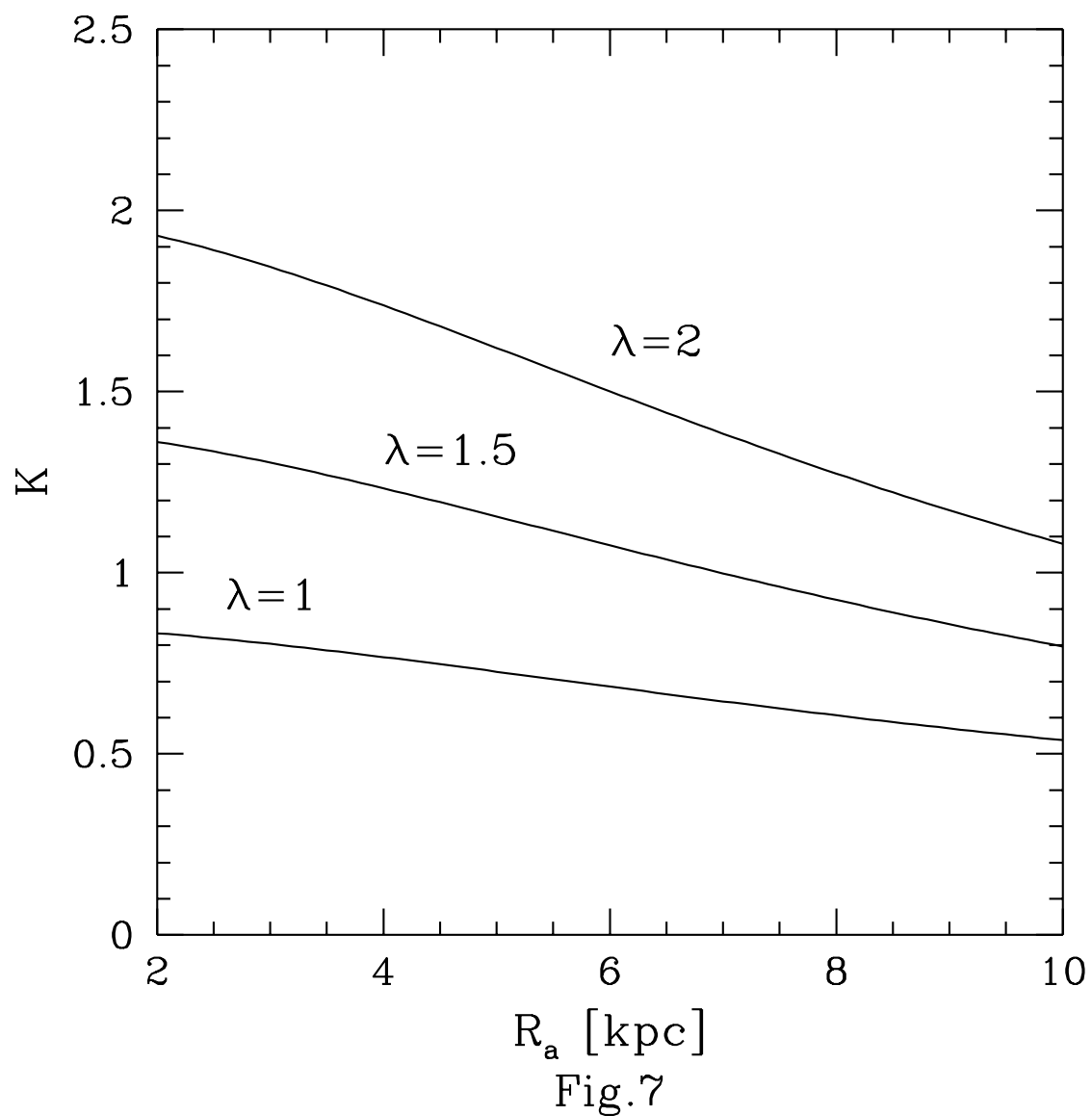


Fig.6



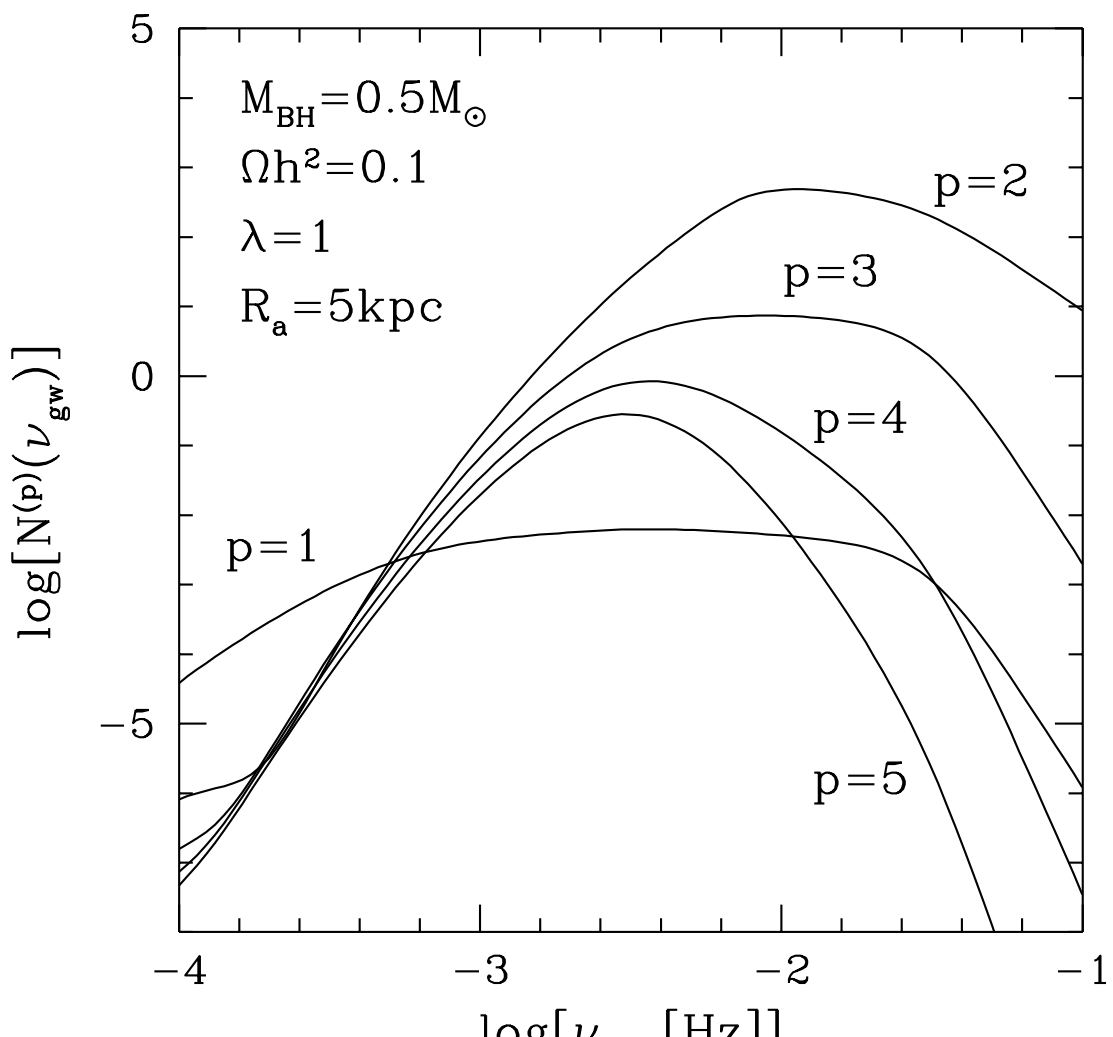


Fig.8

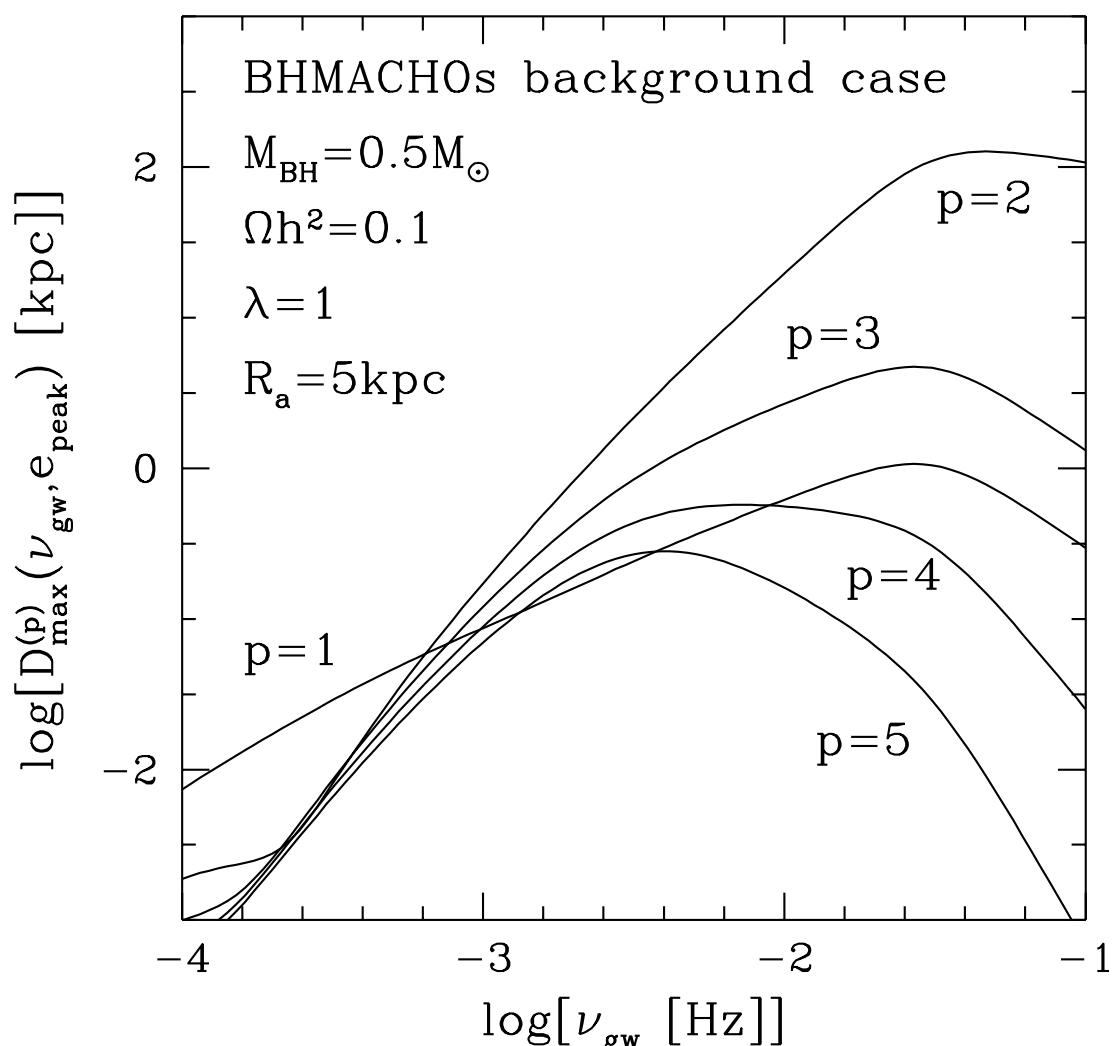


Fig.9

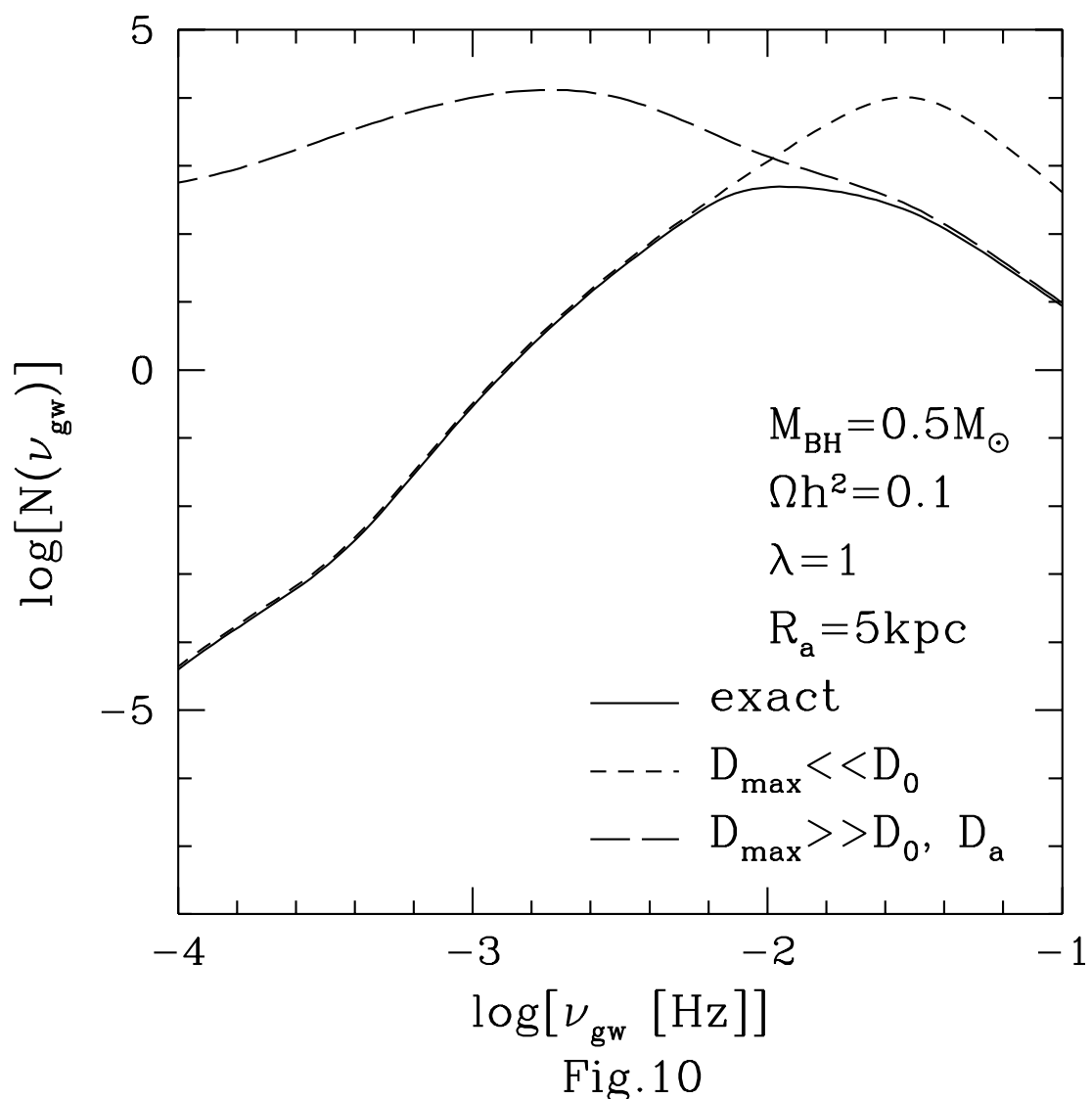


Fig.10

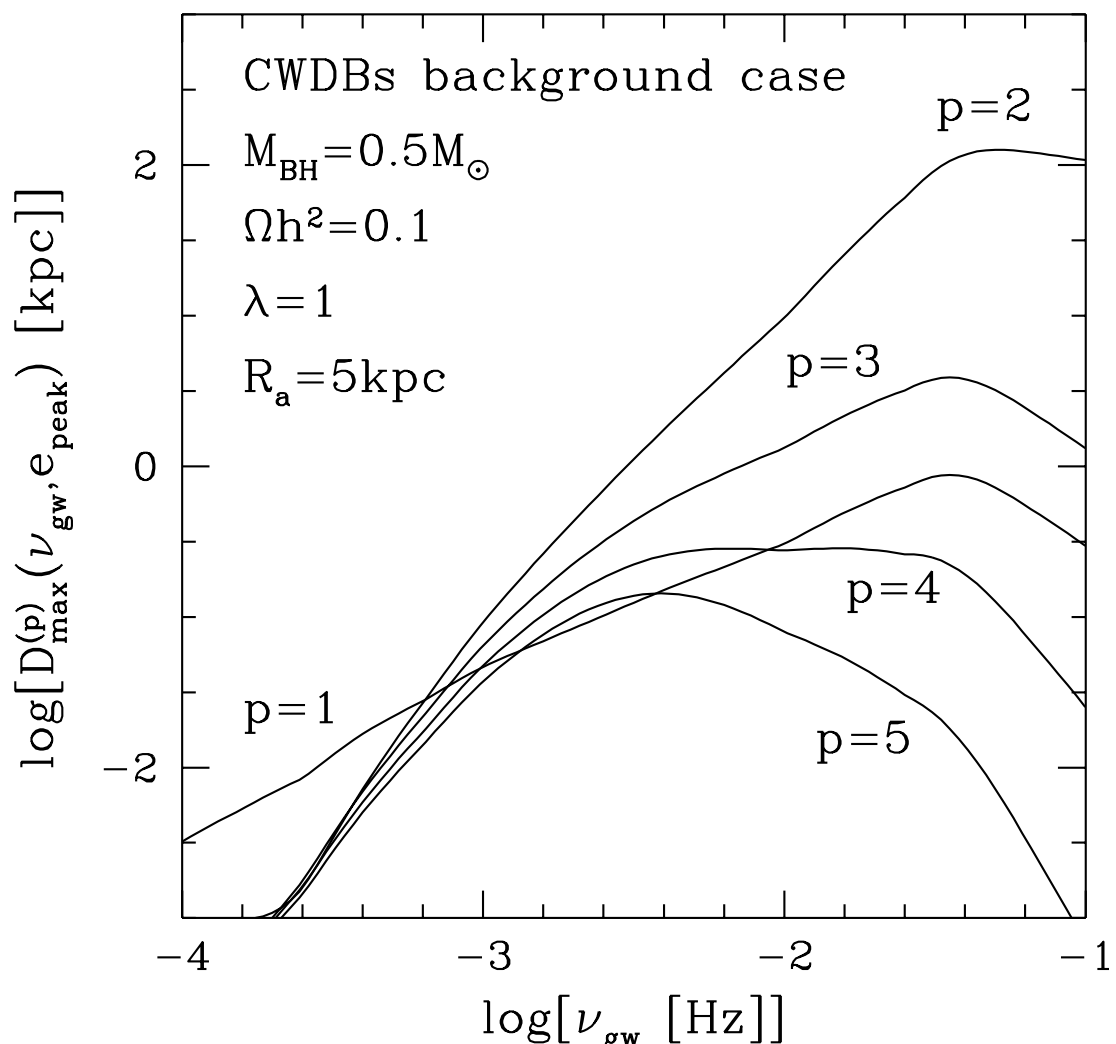


Fig.11

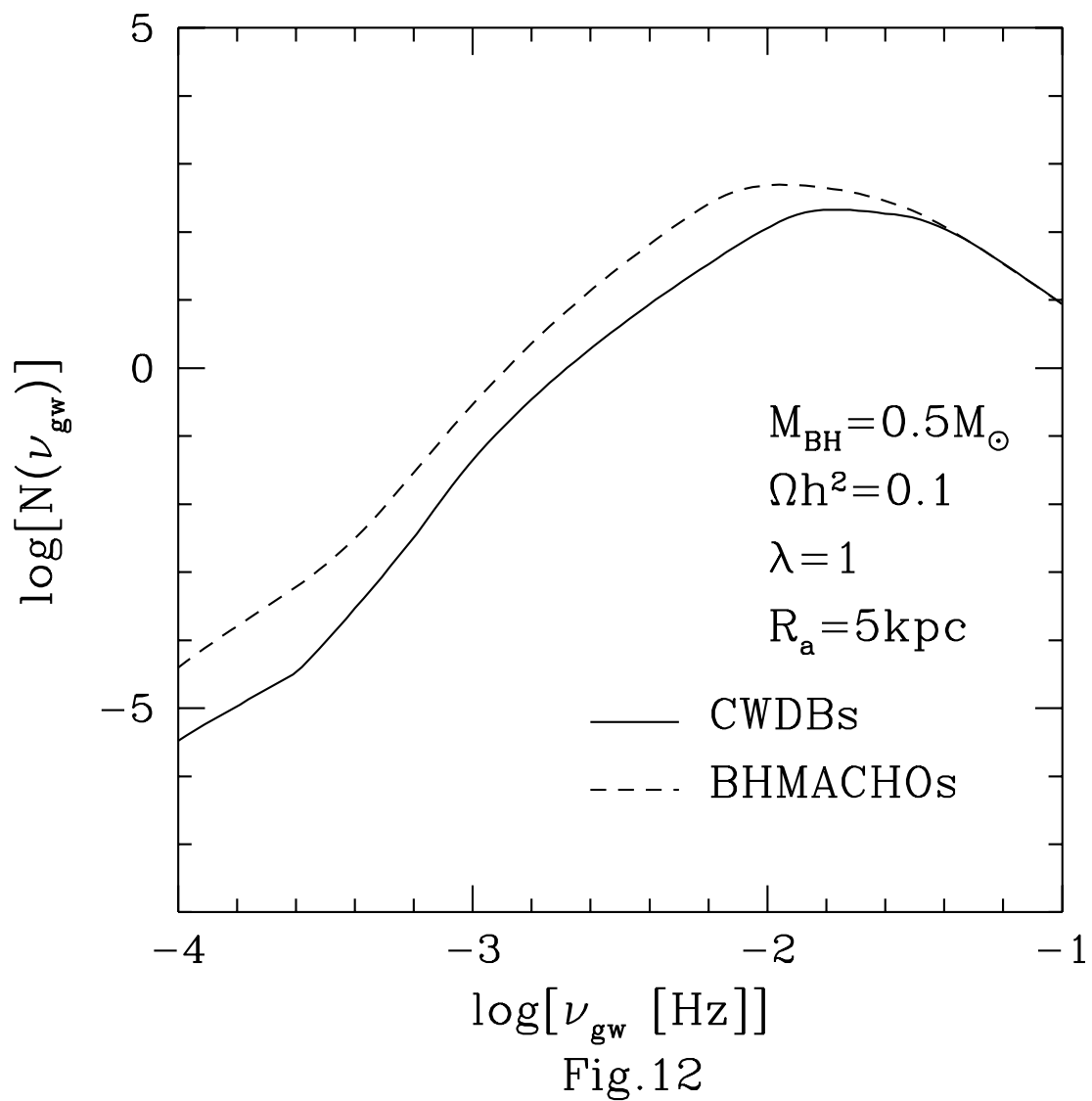


Fig.12

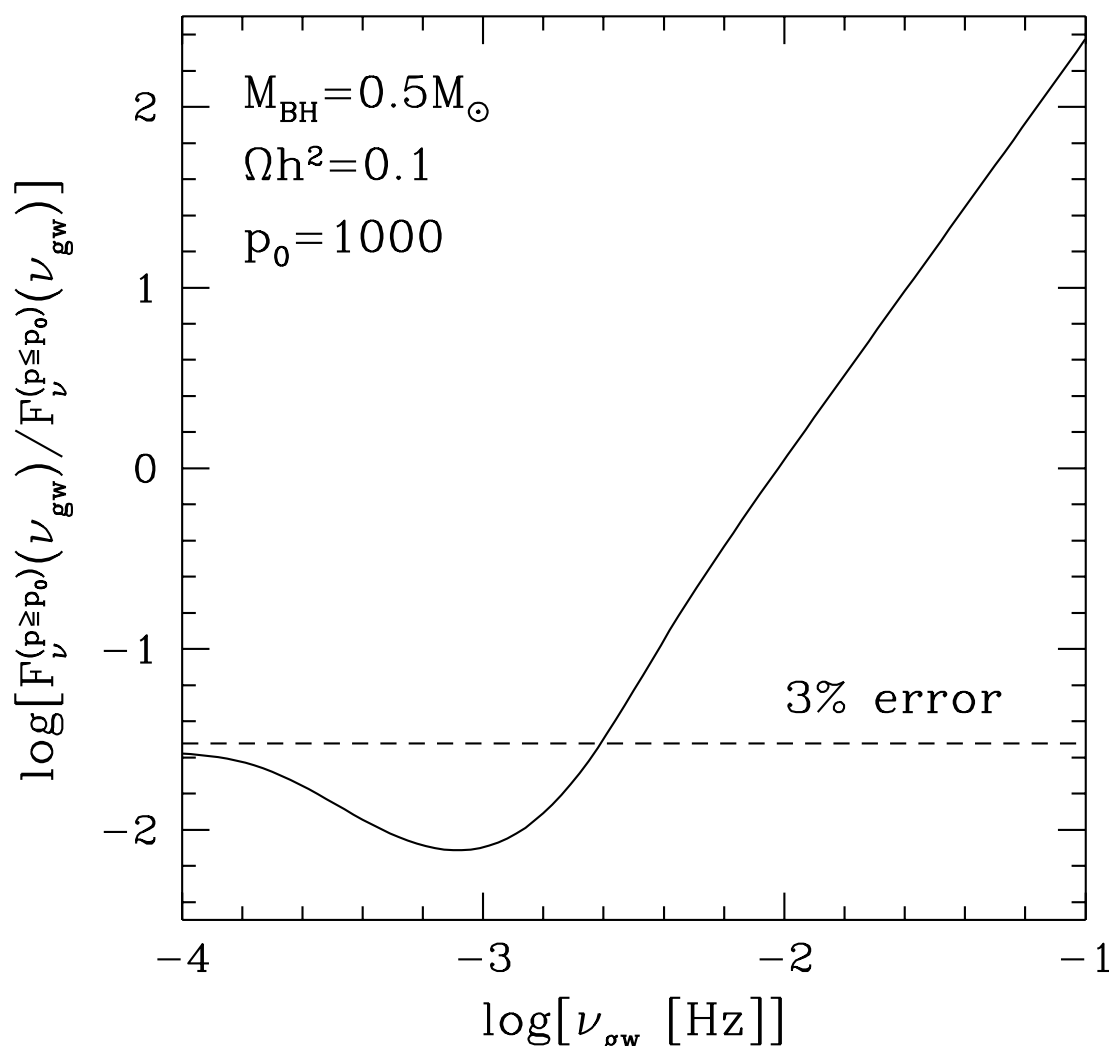


Fig.13